$\Lambda_b \to \Lambda\,\ell^+\ell^-$ form factors, differential branching fraction, and angular observables from lattice QCD with relativistic b quarks

William Detmold[1] and Stefan Meinel[2,3,*]

[1] *Center for Theoretical Physics, Massachusetts Institute of Technology, Cambridge, MA 02139, USA*
[2] *Department of Physics, University of Arizona, Tucson, AZ 85721, USA*
[3] *RIKEN BNL Research Center, Brookhaven National Laboratory, Upton, NY 11973, USA*

(Dated: February 4, 2016)

Using $(2+1)$-flavor lattice QCD, we compute the 10 form factors describing the $\Lambda_b \to \Lambda$ matrix elements of the $b \to s$ vector, axial vector, and tensor currents. The calculation is based on gauge field ensembles generated by the RBC and UKQCD Collaborations with a domain-wall action for the u, d, and s quarks and the Iwasaki gauge action. The b quark is implemented using an anisotropic clover action, tuned nonperturbatively to the physical point, and the currents are renormalized with a mostly nonperturbative method. We perform simultaneous chiral, continuum, and kinematic extrapolations of the form factors through modified z expansions. Using our form factor results, we obtain precise predictions for the $\Lambda_b \to \Lambda(\to p^+\pi^-)\,\mu^+\mu^-$ differential branching fraction and angular observables in the Standard Model.

arXiv:1602.01399v1 [hep-lat] 3 Feb 2016

I. INTRODUCTION

Decays of bottom hadrons involving the flavor-changing neutral-current transition $b \to s\,\ell^+\ell^-$ are sensitive probes of physics beyond the Standard Model. The properties of multiple exclusive $b \to s\,\ell^+\ell^-$ decay channels have been measured with unprecedented precision at the Large Hadron Collider [1], and further substantial increases in statistics are expected in the near future. Some tensions between the experimental data and calculations in the Standard Model have been found, including in the $B \to K^*(\to K\,\pi)\mu^+\mu^-$ angular distribution [2–4], the $B \to K^{(*)}\mu^+\mu^-$ and $B_s \to \phi\mu^+\mu^-$ differential decay rates [5–11], and the ratio R_K of $B \to K\mu^+\mu^-$ and $B \to Ke^+e^-$ decay rates [12]. Global fits of all relevant B and B_s meson decay modes show that a better agreement with the data can be obtained if the Wilson coefficient C_9 in the $b \to s\,\mu^+\mu^-$ effective Hamiltonian is shifted by approximately -25% from its Standard-Model value (other scenarios involving deviations in multiple Wilson coefficients have also been considered) [13, 14]. However, with the exception of R_K, the decay observables are strongly affected by hadronic physics, and it is important to carefully examine all sources of the theory uncertainties. The hadronic contributions include local matrix elements of the $b \to s$ tensor, vector, and axial vector currents from the operators $O_{7,9,10}$ in the effective Hamiltonian, as well as nonlocal matrix elements of products of the operators $O_{1\text{-}6;8}$ with the quark electromagnetic current. The local hadronic matrix elements are expressed in terms of form factors, and can be calculated directly using lattice QCD [15–18]. The treatment of the nonlocal hadronic matrix elements is significantly more challenging, and is usually based on an operator product expansion at high q^2 [19, 20], and QCD factorization [21] combined with light-cone sum rules [22, 23] at low q^2. A particular problem is that the contributions from O_1 and O_2 are enhanced by a multitude of charmonium resonances, with unexpectedly large deviations from naive factorization [24], and can mimic a shift in C_9. To distinguish an apparent shift in C_9 caused by uncontrolled charm contributions from a shift due to new physics, one can study its q^2-dependence [25] and compare the effects seen in multiple different decay modes.

The baryonic decay mode $\Lambda_b \to \Lambda(\to p\,\pi)\ell^+\ell^-$ [26–28] can shed new light on these puzzles. Similarly to $B \to K^*(\to K\,\pi)\ell^+\ell^-$, this decay provides a wealth of angular observables that can be used to disentangle the contributions from individual operators in the $b \to s\,\ell^+\ell^-$ effective Hamiltonian [29, 30] (see also Refs. [31–44]). The theoretical description of $\Lambda_b \to \Lambda(\to p\,\pi)\ell^+\ell^-$ is cleaner than that of $B \to K^*(\to K\,\pi)\ell^+\ell^-$ because the Λ is stable under the strong interactions. The $\Lambda_b \to \Lambda$ form factors are thus "gold-plated" quantities for lattice QCD that can be calculated to high precision using standard methods. In contrast, a rigorous analysis of $B \to K^*(\to K\,\pi)\ell^+\ell^-$ would require the computation of $B \to K\pi$ matrix elements; lattice methods for $1 \to 2$ transition form factors have recently been developed [45–47], but numerical results for $B \to K\pi$ are not yet available. Besides these simplifications in terms of the hadronic physics, the angular distribution of the decay $\Lambda_b \to \Lambda(\to p\,\pi)\ell^+\ell^-$ is sensitive to new combinations of Wilson coefficients that do not appear in $B \to K^*(\to K\,\pi)\ell^+\ell^-$; this is a consequence of parity violation in the secondary weak decay $\Lambda \to p\,\pi$ [30]. A further difference compared to the B decays is the nonzero spin of the initial

* smeinel@email.arizona.edu

hadron. While the Λ_b polarization at LHCb was found to be small and consistent with zero [48], in principle, decays of polarized Λ_b baryons give access to even more observables (taking into account the Λ_b polarization direction, the decay distribution of $\Lambda_b \to \Lambda(\to p\,\pi)\ell^+\ell^-$ depends on five angles [49]). Finally, just like the mesonic $b \to s\,\ell^+\ell^-$ decays, the baryonic mode $\Lambda_b \to \Lambda(\to p\,\pi)\ell^+\ell^-$ is affected by charmonium resonances, which may contribute here with different phases, providing a new handle on this difficult issue.

Given all of these motivations, there is clearly a need for precise determinations of the $\Lambda_b \to \Lambda$ form factors. These form factors have been studied using continuum-based methods in Refs. [29, 34, 39, 41, 43, 50–62]. In Ref. [15], we published a first lattice QCD calculation of the $\Lambda_b \to \Lambda$ form factors, where the b quark was treated at leading order in heavy-quark effective theory to simplify the analysis. In the following, we present a new lattice QCD calculation in which we do not make this approximation (early progress was shown in Ref. [63]). Using a relativistic heavy-quark action [64–68], we now work directly at the physical b quark mass and compute all 10 QCD form factors describing the $\Lambda_b \to \Lambda$ matrix elements of the $b \to s$ vector, axial vector, and tensor currents. The methods closely follow Ref. [69], where we computed the $\Lambda_b \to p$ and $\Lambda_b \to \Lambda_c$ form factors that were used in Ref. [70] to determine the ratio $|V_{ub}/V_{cb}|$ from the decays $\Lambda_b \to p\,\mu^-\bar{\nu}_\mu$ and $\Lambda_b \to \Lambda_c\,\mu^-\bar{\nu}_\mu$ at the LHC. Our lattice calculations utilize a domain-wall action [71–73] for the u, d, and s quarks, and are based on gauge field ensembles generated by the RBC and UKQCD Collaborations [74].

We proceed by summarizing the relevant definitions of the $\Lambda_b \to \Lambda$ form factors in Sec. II, before presenting our computation of the form factors on the lattice in Sec. III. We discuss the fits of the form factors using the modified z expansion and the estimates of systematic uncertainties in Sec. IV. Our predictions for the $\Lambda_b \to \Lambda(\to p\,\pi)\mu^+\mu^-$ differential branching fraction and angular observables are given in Sec. V.

II. DEFINITIONS OF THE FORM FACTORS

In this work, we mainly use the helicity-based definition of the form factors from Ref. [59], which is given by

$$\begin{aligned}
\langle \Lambda(p',s')|\bar{s}\,\gamma^\mu\, b|\Lambda_b(p,s)\rangle &= \bar{u}_\Lambda(p',s')\bigg[f_0(q^2)\,(m_{\Lambda_b}-m_\Lambda)\frac{q^\mu}{q^2} \\
&\quad + f_+(q^2)\frac{m_{\Lambda_b}+m_\Lambda}{s_+}\left(p^\mu + p'^\mu - (m^2_{\Lambda_b}-m^2_\Lambda)\frac{q^\mu}{q^2}\right) \\
&\quad + f_\perp(q^2)\left(\gamma^\mu - \frac{2m_\Lambda}{s_+}p^\mu - \frac{2m_{\Lambda_b}}{s_+}p'^\mu\right)\bigg] u_{\Lambda_b}(p,s), \qquad (1)\\
\langle \Lambda(p',s')|\bar{s}\,\gamma^\mu\gamma_5\, b|\Lambda_b(p,s)\rangle &= -\bar{u}_\Lambda(p',s')\,\gamma_5\bigg[g_0(q^2)\,(m_{\Lambda_b}+m_\Lambda)\frac{q^\mu}{q^2} \\
&\quad + g_+(q^2)\frac{m_{\Lambda_b}-m_\Lambda}{s_-}\left(p^\mu + p'^\mu - (m^2_{\Lambda_b}-m^2_\Lambda)\frac{q^\mu}{q^2}\right) \\
&\quad + g_\perp(q^2)\left(\gamma^\mu + \frac{2m_\Lambda}{s_-}p^\mu - \frac{2m_{\Lambda_b}}{s_-}p'^\mu\right)\bigg] u_{\Lambda_b}(p,s), \qquad (2)\\
\langle \Lambda(p',s')|\bar{s}\,i\sigma^{\mu\nu}q_\nu\, b|\Lambda_b(p,s)\rangle &= -\bar{u}_\Lambda(p',s')\bigg[h_+(q^2)\frac{q^2}{s_+}\left(p^\mu + p'^\mu - (m^2_{\Lambda_b}-m^2_\Lambda)\frac{q^\mu}{q^2}\right) \\
&\quad + h_\perp(q^2)\,(m_{\Lambda_b}+m_\Lambda)\left(\gamma^\mu - \frac{2m_\Lambda}{s_+}\,p^\mu - \frac{2m_{\Lambda_b}}{s_+}\,p'^\mu\right)\bigg] u_{\Lambda_b}(p,s), \qquad (3)\\
\langle \Lambda(p',s')|\bar{s}\,i\sigma^{\mu\nu}q_\nu\gamma_5\, b|\Lambda_b(p,s)\rangle &= -\bar{u}_\Lambda(p',s')\,\gamma_5\bigg[\widetilde{h}_+(q^2)\,\frac{q^2}{s_-}\left(p^\mu + p'^\mu - (m^2_{\Lambda_b}-m^2_\Lambda)\frac{q^\mu}{q^2}\right) \\
&\quad + \widetilde{h}_\perp(q^2)\,(m_{\Lambda_b}-m_\Lambda)\left(\gamma^\mu + \frac{2m_\Lambda}{s_-}\,p^\mu - \frac{2m_{\Lambda_b}}{s_-}\,p'^\mu\right)\bigg] u_{\Lambda_b}(p,s), \qquad (4)
\end{aligned}$$

with $q = p - p'$, $\sigma^{\mu\nu} = \frac{i}{2}(\gamma^\mu\gamma^\nu - \gamma^\nu\gamma^\mu)$ and $s_\pm = (m_{\Lambda_b} \pm m_\Lambda)^2 - q^2$. The helicity form factors describe the contractions of the matrix elements with virtual polarization vectors that are given explicitly in Ref. [30] (note that Ref. [30] uses different labels for the form factors, which are related to the notation of Ref. [59] adopted here as follows: $f_t^V = f_0$, $f_0^V = f_+$, $f_\perp^V = f_\perp$, $f_t^A = g_0$, $f_0^A = g_+$, $f_\perp^A = g_\perp$, $f_0^T = h_+$, $f_\perp^T = h_\perp$, $f_0^{T5} = \widetilde{h}_+$, $f_\perp^{T5} = \widetilde{h}_\perp$). The helicity form factors

satisfy the endpoint relations

$$f_0(0) = f_+(0), \tag{5}$$
$$g_0(0) = g_+(0), \tag{6}$$
$$g_\perp(q^2_{\rm max}) = g_+(q^2_{\rm max}), \tag{7}$$
$$\widetilde{h}_\perp(q^2_{\rm max}) = \widetilde{h}_+(q^2_{\rm max}), \tag{8}$$

where $q^2_{\rm max} = (m_{\Lambda_b} - m_\Lambda)^2$. As in Ref. [69], in some parts of our data analysis we simultaneously work with an alternative basis that decomposes the matrix elements into form factors of the first and second class according to Weinberg's classification [75], and is given by [29]

$$\langle \Lambda(p',s')|\bar{s}\,\gamma^\mu\, b|\Lambda_b(p,s)\rangle = \bar{u}_\Lambda(p',s')\left[f_1^V(q^2)\,\gamma^\mu - \frac{f_2^V(q^2)}{m_{\Lambda_b}} i\sigma^{\mu\nu}q_\nu + \frac{f_3^V(q^2)}{m_{\Lambda_b}} q^\mu\right] u_{\Lambda_b}(p,s), \tag{9}$$

$$\langle \Lambda(p',s')|\bar{s}\,\gamma^\mu\gamma_5\, b|\Lambda_b(p,s)\rangle = \bar{u}_\Lambda(p',s')\left[f_1^A(q^2)\,\gamma^\mu - \frac{f_2^A(q^2)}{m_{\Lambda_b}} i\sigma^{\mu\nu}q_\nu + \frac{f_3^A(q^2)}{m_{\Lambda_b}} q^\mu\right] \gamma_5\, u_{\Lambda_b}(p,s), \tag{10}$$

$$\langle \Lambda(p',s')|\bar{s}\,i\sigma^{\mu\nu}q_\nu\, b|\Lambda_b(p,s)\rangle = \bar{u}_\Lambda(p',s')\left[\frac{f_1^{TV}(q^2)}{m_{\Lambda_b}}\left(\gamma^\mu q^2 - q^\mu \not{q}\right) - f_2^{TV}(q^2) i\sigma^{\mu\nu}q_\nu\right] u_{\Lambda_b}(p,s), \tag{11}$$

$$\langle \Lambda(p',s')|\bar{s}\,i\sigma^{\mu\nu}q_\nu\,\gamma_5\, b|\Lambda_b(p,s)\rangle = \bar{u}_\Lambda(p',s')\left[\frac{f_1^{TA}(q^2)}{m_{\Lambda_b}}\left(\gamma^\mu q^2 - q^\mu \not{q}\right) - f_2^{TA}(q^2) i\sigma^{\mu\nu}q_\nu\right] \gamma_5\, u_{\Lambda_b}(p,s). \tag{12}$$

These "Weinberg form factors" are related to the helicity form factors introduced above as follows:

$$f_+(q^2) = f_1^V(q^2) + \frac{q^2}{m_{\Lambda_b}(m_{\Lambda_b}+m_\Lambda)} f_2^V(q^2), \tag{13}$$
$$f_\perp(q^2) = f_1^V(q^2) + \frac{m_{\Lambda_b}+m_\Lambda}{m_{\Lambda_b}} f_2^V(q^2), \tag{14}$$
$$f_0(q^2) = f_1^V(q^2) + \frac{q^2}{m_{\Lambda_b}(m_{\Lambda_b}-m_\Lambda)} f_3^V(q^2), \tag{15}$$
$$g_+(q^2) = f_1^A(q^2) - \frac{q^2}{m_{\Lambda_b}(m_{\Lambda_b}-m_\Lambda)} f_2^A(q^2), \tag{16}$$
$$g_\perp(q^2) = f_1^A(q^2) - \frac{m_{\Lambda_b}-m_\Lambda}{m_{\Lambda_b}} f_2^A(q^2), \tag{17}$$
$$g_0(q^2) = f_1^A(q^2) - \frac{q^2}{m_{\Lambda_b}(m_{\Lambda_b}+m_\Lambda)} f_3^A(q^2), \tag{18}$$
$$h_+(q^2) = -f_2^{TV}(q^2) - \frac{m_{\Lambda_b}+m_\Lambda}{m_{\Lambda_b}} f_1^{TV}(q^2), \tag{19}$$
$$h_\perp(q^2) = -f_2^{TV}(q^2) - \frac{q^2}{m_{\Lambda_b}(m_{\Lambda_b}+m_\Lambda)} f_1^{TV}(q^2), \tag{20}$$
$$\widetilde{h}_+(q^2) = -f_2^{TA}(q^2) + \frac{m_{\Lambda_b}-m_\Lambda}{m_{\Lambda_b}} f_1^{TA}(q^2), \tag{21}$$
$$\widetilde{h}_\perp(q^2) = -f_2^{TA}(q^2) + \frac{q^2}{m_{\Lambda_b}(m_{\Lambda_b}-m_\Lambda)} f_1^{TA}(q^2). \tag{22}$$

III. LATTICE CALCULATION

The lattice calculation was performed using the same actions, parameters, and analysis methods as in Ref. [69], with a few modifications to accommodate the Λ final state and the tensor currents as explained in the following. The strange quark was implemented using the same domain-wall action as the up and down quarks, with masses given in Table I. We used the interpolating field

$$\Lambda_\alpha = \epsilon^{abc}\,(C\gamma_5)_{\beta\gamma}\,\widetilde{d}^a_\beta\,\widetilde{u}^b_\gamma\,\widetilde{s}^c_\alpha \tag{23}$$

for the Λ baryon, with smearing parameters $(\sigma, n_S) = (4.35, 30)$ for all three quark fields [69, 76]. The renormalized, $\mathcal{O}(a)$-improved $b \to s$ vector and axial vector currents are defined as in Eqs. (18)-(21) of Ref. [69], with matching

Set	β	$N_s^3 \times N_t$	$am_s^{(\mathrm{sea})}$	$am_{u,d}^{(\mathrm{sea})}$	a [fm]	$am_{u,d}^{(\mathrm{val})}$	$m_\pi^{(\mathrm{val})}$ [MeV]	$am_s^{(\mathrm{val})}$	$m_{\eta_s}^{(\mathrm{val})}$ [MeV]	N_{meas}
C14	2.13	$24^3 \times 64$	0.04	0.005	0.1119(17)	0.001	245(4)	0.04	761(12)	2672
C24	2.13	$24^3 \times 64$	0.04	0.005	0.1119(17)	0.002	270(4)	0.04	761(12)	2676
C54	2.13	$24^3 \times 64$	0.04	0.005	0.1119(17)	0.005	336(5)	0.04	761(12)	2782
C53	2.13	$24^3 \times 64$	0.04	0.005	0.1119(17)	0.005	336(5)	0.03	665(10)	1205
F23	2.25	$32^3 \times 64$	0.03	0.004	0.0849(12)	0.002	227(3)	0.03	747(10)	1907
F43	2.25	$32^3 \times 64$	0.03	0.004	0.0849(12)	0.004	295(4)	0.03	747(10)	1917
F63	2.25	$32^3 \times 64$	0.03	0.006	0.0848(17)	0.006	352(7)	0.03	749(14)	2782

TABLE I. Parameters of the seven data sets used in this work. The quark masses $am_{u,d}^{(\mathrm{sea})}$ and $am_s^{(\mathrm{sea})}$ were used in the generation of the ensembles [74], while the quark masses $am_{u,d}^{(\mathrm{val})}$ and $am_s^{(\mathrm{val})}$ were used in the computation of the propagators. The resulting pion and η_s masses are denoted as $m_\pi^{(\mathrm{val})}$ and $m_{\eta_s}^{(\mathrm{val})}$. The η_s is an artificial pseudoscalar $s\bar{s}$ meson that is obtained by treating the s and $\bar{s}$ as different, but mass-degenerate flavors. We use this state as an intermediate quantity to tune the strange-quark mass [79]; the η_s mass at the physical point has been computed precisely by the HPQCD collaboration and is $m_{\eta_s}^{(\mathrm{phys})} = 689.3(1.2)\,\mathrm{MeV}$ [80]. The values of the lattice spacing, a, were taken from Ref. [81]. The parameters of the anisotropic clover action used for the bottom quark can be found in Ref. [68].

coefficients equal to those for $b \to u$ (see Table III of Ref. [69]). For the tensor current, we also use the mostly nonperturbative renormalization method introduced in Refs. [77, 78], but we set the residual matching factors and $\mathcal{O}(a)$-improvement coefficients to their mean-field-improved tree-level values (because one-loop results were not available). That is, we write the tensor current as

$$T_{\mu\nu} = \sqrt{Z_V^{(ss)} Z_V^{(bb)}} \Big[\bar{s}\sigma_{\mu\nu} b + a\, d_1 \sum_{j=1}^{3} \bar{s}\sigma_{\mu\nu}\gamma_j \overrightarrow{\nabla}_j b \Big], \tag{24}$$

with $Z_V^{(bb)}$ and $Z_V^{(ss)} = Z_V^{(uu)}$ as given in Table IV of Ref. [69], and with $d_1 = 0.0740$ for the coarse lattice spacing and $d_1 = 0.0718$ for the fine lattice spacing (for d_1, we use the averages of the values computed with u_0 from either the Landau-gauge mean link or the plaquette). As discussed in Secs. IV and V, this approximation introduces a systematic uncertainty of approximately 5% in the tensor form factors, which however has negligible impact on the $\Lambda_b \to \Lambda(\to p\,\pi)\mu^+\mu^-$ observables.

The extraction of the form factors from ratios of three-point and two-point functions is performed as in Ref. [69]. In addition to the ratios $\mathscr{R}_{+,\perp,0}^{V,A}(\mathbf{p}', t, t')$ for the vector and axial vector currents, given in Eqs. (46)-(48) of Ref. [69], we now define

$$\mathscr{R}_{+}^{TV}(\mathbf{p}', t, t') = \frac{r_\mu[(1,\mathbf{0})]\, r_\nu[(1,\mathbf{0})]\, \mathrm{Tr}\Big[C^{(3,\mathrm{fw})}(\mathbf{p}',\, i\sigma^{\mu\rho}q_\rho, t, t')\, C^{(3,\mathrm{bw})}(\mathbf{p}',\, i\sigma^{\nu\lambda}q_\lambda, t, t-t')\Big]}{\mathrm{Tr}\Big[C^{(2,\Lambda,\mathrm{av})}(\mathbf{p}', t)\Big]\, \mathrm{Tr}\Big[C^{(2,\Lambda_b,\mathrm{av})}(t)\Big]}, \tag{25}$$

$$\mathscr{R}_{\perp}^{TV}(\mathbf{p}', t, t') = \frac{r_\mu[(0,\mathbf{e}_j\times\mathbf{p}')]\, r_\nu[(0,\mathbf{e}_k\times\mathbf{p}')]\, \mathrm{Tr}\Big[C^{(3,\mathrm{fw})}(\mathbf{p}',\, i\sigma^{\mu\rho}q_\rho, t, t')\gamma_5\gamma^j\, C^{(3,\mathrm{bw})}(\mathbf{p}',\, i\sigma^{\nu\lambda}q_\lambda, t, t-t')\gamma_5\gamma^k\Big]}{\mathrm{Tr}\Big[C^{(2,\Lambda,\mathrm{av})}(\mathbf{p}', t)\Big]\, \mathrm{Tr}\Big[C^{(2,\Lambda_b,\mathrm{av})}(t)\Big]}, \tag{26}$$

where the current $iT^{\mu\nu}q_\nu$ is used in the three-point functions, as well as the ratios $\mathscr{R}_{+,\perp}^{TA}(\mathbf{p}', t, t')$ with the replacement $\sigma^{\mu\nu} \mapsto \sigma^{\mu\nu}\gamma_5$ in the current. Here, $\mathbf{p}'$ is the spatial momentum of the Λ baryon, t is the source-sink separation, and t' is the time at which the current is inserted in the three-point function [69]. We average the data at fixed $|\mathbf{p}'|$ over the directions of $\mathbf{p}'$, and denote the direction-averaged ratios by $\mathscr{R}_{+,\perp,0}^{V,A}(|\mathbf{p}'|, t, t')$, $\mathscr{R}_{+,\perp}^{TV,TA}(|\mathbf{p}'|, t, t')$. As in Ref. [69], we generated data for all source-sink separations in the range $t/a = 4...15$ (C14, C24, C54, C53 data sets), $t/a = 5...15$ (F23, F43 data sets), and $t/a = 5...17$ (F63 data set). Examples of numerical results for $\mathscr{R}_{+,\perp,0}^{V,A}(|\mathbf{p}'|, t, t')$, $\mathscr{R}_{+,\perp}^{TV,TA}(|\mathbf{p}'|, t, t')$ from the C24 data set are shown in Fig. 1. We then evaluate these ratios at the midpoint $t' = t/2$ (or, in the case of odd t/a, average over $t' = (t-a)/2$ and $t' = (t+a)/2$), and compute the quantities $R_{f_+}(|\mathbf{p}'|, t)$, $R_{f_\perp}(|\mathbf{p}'|, t)$, $R_{f_0}(|\mathbf{p}'|, t)$, $R_{g_+}(|\mathbf{p}'|, t)$, $R_{g_\perp}(|\mathbf{p}'|, t)$, $R_{g_0}(|\mathbf{p}'|, t)$, which are defined as in Eqs. (52), (53), (54), (58), (59),

Set	am_{Λ_b}	am_{Λ}	am_{B_s}	am_B
C14	3.305(11)	0.7064(38)	3.1135(11)	3.0649(27)
C24	3.299(10)	0.7159(37)	3.1117(11)	3.0628(29)
C54	3.3161(71)	0.7348(30)	3.1115(11)	3.0638(33)
C53	3.3257(92)	0.7096(47)	3.0994(14)	3.0682(43)
F23	2.469(16)	0.5190(42)	2.3546(16)	2.3198(32)
F43	2.492(11)	0.5354(29)	2.3542(16)	2.3230(26)
F63	2.5089(70)	0.5514(23)	2.3554(11)	2.3221(22)

TABLE II. Hadron masses in lattice units.

(60) of Ref. [69], and

$$R_{h_+}(|\mathbf{p}'|,t) = \frac{2}{E_\Lambda - m_\Lambda}\sqrt{\frac{E_\Lambda}{(E_\Lambda+m_\Lambda)}\mathscr{R}_+^{TV}(|\mathbf{p}'|,t,t/2)}, \tag{27}$$

$$R_{h_\perp}(|\mathbf{p}'|,t) = \frac{1}{(E_\Lambda - m_\Lambda)(m_{\Lambda_b}+m_\Lambda)}\sqrt{\frac{E_\Lambda}{E_\Lambda+m_\Lambda}\mathscr{R}_\perp^{TV}(|\mathbf{p}'|,t,t/2)}, \tag{28}$$

$$R_{\widetilde{h}_+}(|\mathbf{p}'|,t) = \frac{2}{E_\Lambda + m_\Lambda}\sqrt{\frac{E_\Lambda}{E_\Lambda - m_\Lambda}\mathscr{R}_+^{TA}(|\mathbf{p}'|,t,t/2)}, \tag{29}$$

$$R_{\widetilde{h}_\perp}(|\mathbf{p}'|,t) = \frac{1}{(E_\Lambda + m_\Lambda)(m_{\Lambda_b}-m_\Lambda)}\sqrt{-\frac{E_\Lambda}{E_\Lambda - m_\Lambda}\mathscr{R}_\perp^{TA}(|\mathbf{p}'|,t,t/2)}. \tag{30}$$

These quantities are equal to the desired helicity form factors at the given momentum and lattice parameters, up to excited-state contamination that decays exponentially with the source-sink separation, t. Here, we use bootstrap samples for the lattice baryon masses, am_{Λ_b} and am_Λ, from fits to the two-point functions of the individual data sets (see Table II), and compute the energies aE_Λ at nonzero momentum using the relativistic continuum dispersion relation. Following Ref. [69], we also constructed the linear combinations of the above quantities that yield the Weinberg form factors by inverting Eqs. (13)-(22), for example

$$R_{f_2^{TV}}(|\mathbf{p}'|,t) = \frac{q^2 R_{h_+}(|\mathbf{p}'|,t) - (m_{\Lambda_b}+m_\Lambda)^2 R_{h_\perp}(|\mathbf{p}'|,t)}{s_+}. \tag{31}$$

Denoting the data by $R_{f,i,n}(t)$, where f labels the helicity and Weinberg form factors, $i =$ C14, C24, ... labels the data set, and n labels the Λ-momentum via $|\mathbf{p}'|^2 = n\,(2\pi)^2/L^2$, we then performed fits using the functions

$$R_{f,i,n}(t) = f_{i,n} + A_{f,i,n}\, e^{-\delta_{f,i,n}\, t}, \quad \delta_{f,i,n} = \delta_{\min} + e^{\,l_{f,i,n}}\ \text{GeV}, \tag{32}$$

with parameters $f_{i,n}$, $A_{f,i,n}$, and $l_{f,i,n}$. Here $f_{i,n}$ are the ground-state form factors we aim to extract, and the term with the exponential t-dependence describes the leading excited-state contamination. Writing the energy gaps $\delta_{f,i,n}$ in the above form imposes the constraint $\delta_{f,i,n} > \delta_{\min}$, where we set $\delta_{\min} = 170$ MeV [69]. This constraint has negligible effect in most cases, but prevents numerical instabilities for some form factors at certain momenta where the data show no discernible t-dependence. At each momentum n, we performed one coupled fit to the data for all the vector form factors ($f_{+,\perp,0}$, $f^V_{1,2,3}$), one coupled fit to the data for all the axial vector form factors ($g_{+,\perp,0}$, $f^A_{1,2,3}$), one coupled fit to the data for all the "tensor-vector" form factors ($h_{+,\perp}$, $f^{TV}_{1,2}$), and one coupled fit for all the "tensor-axial-vector" form factors ($\widetilde{h}_{+,\perp}$, $f^{TA}_{1,2}$). As discussed in detail in Ref. [69], in these coupled fits we impose the constraint that the form factor parameters $f_{i,n}$ satisfy the relations (13)-(22), and we include Gaussian priors that limit the variation of the energy gap parameters between the different data sets to reasonable ranges (we generalize Eq. (71) of Ref. [69] to also include strange-quark mass dependence by writing $[\sigma^{i,j}_m]^2 = w_m^2[(m^i_\pi)^2 - (m^j_\pi)^2]^2 + w_m^2[(m^i_{\eta_s})^2 - (m^j_{\eta_s})^2]^2$, with $w_m = 4\ \text{GeV}^{-2}$ as before). Examples of these fits are shown in Fig. 2. Following Ref. [69], we estimated the systematic uncertainties resulting from neglected higher excited states by computing the shifts in $f_{i,n}$ when removing the points with the smallest values of t from the fits, and added these uncertainties in quadrature to the statistical uncertainties. Tables of the extracted lattice form factors are given in Appendix A.

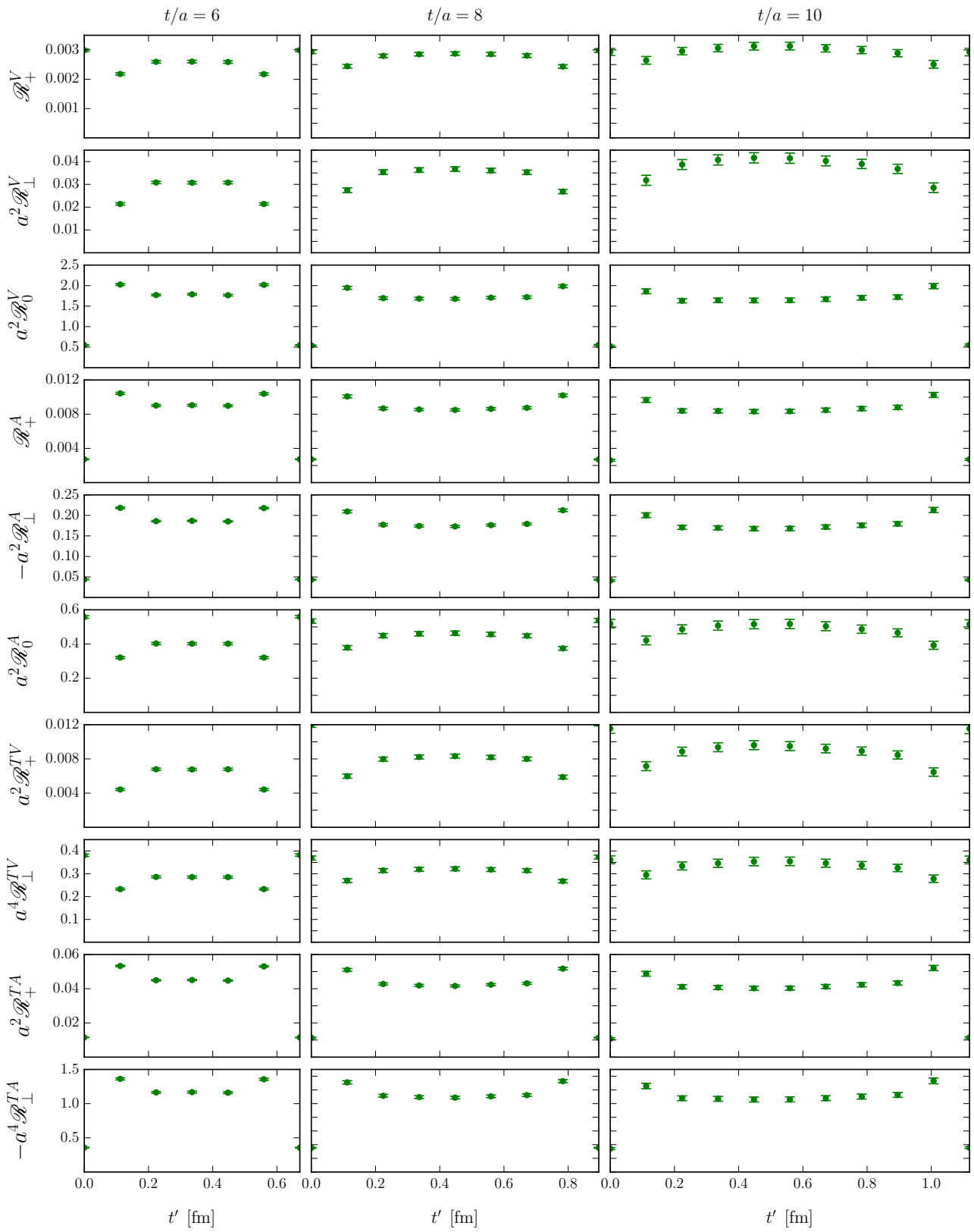

FIG. 1. Examples of numerical results for the ratios $\mathscr{R}^{V,\,A}_{+,\,\perp,\,0}(|\mathbf{p}'|,t,t')$, $\mathscr{R}^{TV,\,TA}_{+,\,\perp}(|\mathbf{p}'|,t,t')$ for three different source-sink separations, plotted as a function of the current insertion time, t'. The data shown here are from the `C24` data set at $|\mathbf{p}'|^2 = 3(2\pi/L)^2$.

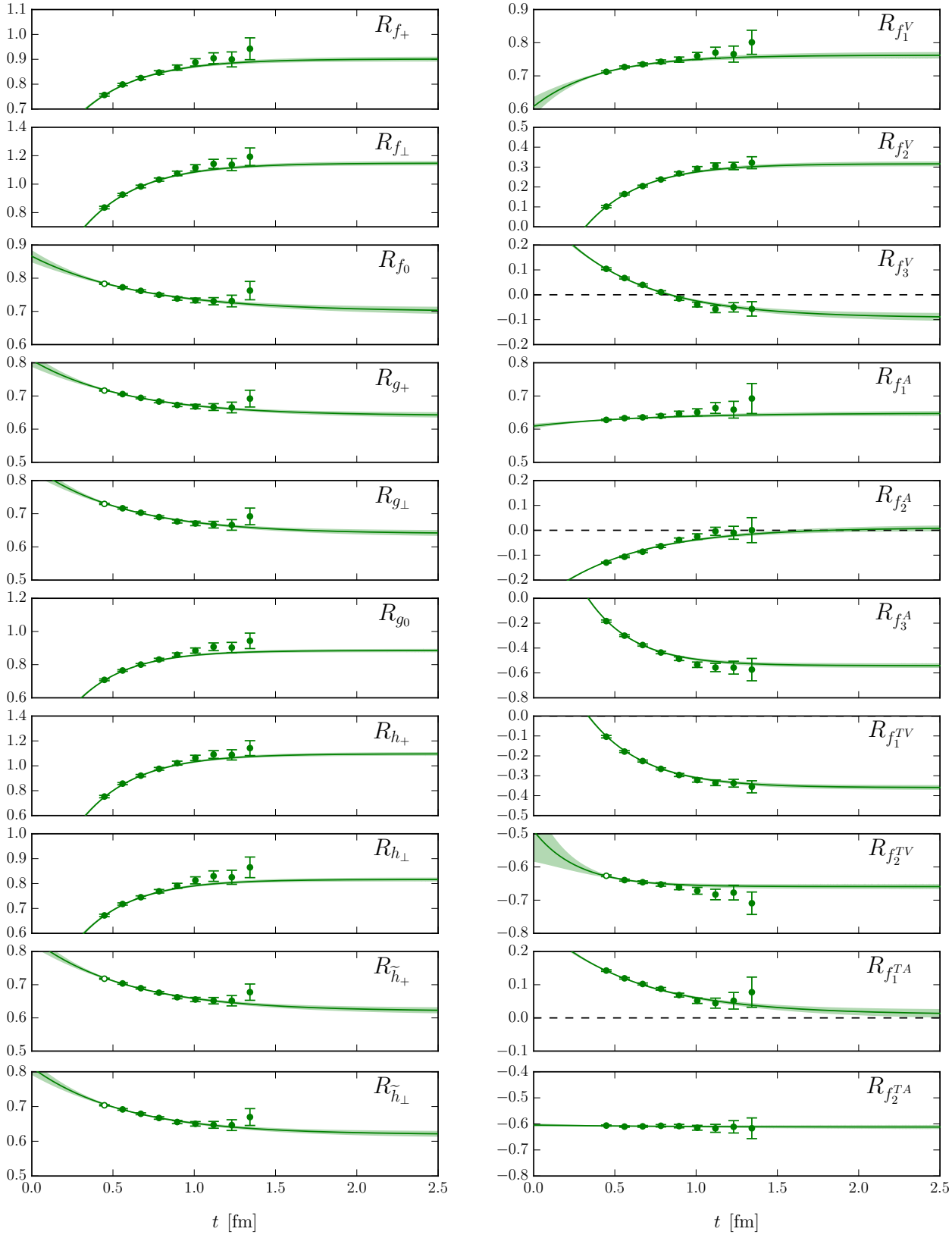

FIG. 2. Examples of fits of the quantities $R_f(|\mathbf{p}'|, t)$ as a function of the source-sink separation, t. These quantities approach the ground-state form factors, f, for large t. The data shown here are from the C24 data set at $|\mathbf{p}'|^2 = 3(2\pi/L)^2$; points plotted with open symbols are excluded from the fit.

IV. CHIRAL/CONTINUUM/KINEMATIC EXTRAPOLATION OF THE FORM FACTORS

To obtain parametrizations of the $\Lambda_b \to \Lambda$ helicity form factors in the physical limit $a = 0$, $m_\pi = m_{\pi,\text{phys}}$, $m_{\eta_s} = m_{\eta_s,\text{phys}}$ (see the caption of Table I), we performed global fits of the lattice data using the simplified z expansion [82], augmented with additional terms that allow for quark-mass and lattice-spacing dependence. In this approach, the q^2-dependence is described by a Taylor expansion in the variable

$$z(q^2) = \frac{\sqrt{t_+ - q^2} - \sqrt{t_+ - t_0}}{\sqrt{t_+ - q^2} + \sqrt{t_+ - t_0}}. \tag{33}$$

Here, t_0 determines the value of q^2 that is mapped to $z = 0$; we set

$$t_0 = q^2_{\text{max}} = (m_{\Lambda_b} - m_\Lambda)^2. \tag{34}$$

Values of q^2 greater than t_+ will be mapped onto the unit circle in the complex z plane. We set t_+ equal to the onset location of the branch cut associated with the $B\,K$ threshold,

$$t_+ = (m_B + m_K)^2. \tag{35}$$

Note that $B_s\,\pi$ intermediate states are forbidden by isospin symmetry, which is exact in our calculation. The three-particle $B_s\,\pi\,\pi$ threshold also lies slightly below the $B\,K$ threshold and is not forbidden by isospin symmetry, but its contributions to dispersive bounds on the z-expansion coefficients are expected to be highly suppressed [83]. Before expanding the form factors in a series in z, we factor out the poles associated with the lowest relevant B_s states; their masses are given in Table III. We find that the lattice data are well described by a fit to first order in z using the functions

$$\begin{aligned} f(q^2) = \frac{1}{1 - q^2/(m^f_{\text{pole}})^2} &\left[a^f_0 \left(1 + c^f_0 \frac{m^2_\pi - m^2_{\pi,\text{phys}}}{\Lambda^2_\chi} + c^f_{s,0} \frac{m^2_{\eta_s} - m^2_{\eta_s,\text{phys}}}{\Lambda^2_\chi}\right) + a^f_1\, z(q^2)\right] \\ &\times \left[1 + b^f\, a^2 |\mathbf{p}'|^2 + d^f\, a^2 \Lambda^2_{\text{QCD}}\right], \end{aligned} \tag{36}$$

with parameters a^f_0, a^f_1, c^f_0, c^f_s, b^f, and d^f. Terms $\sim \mathcal{O}(a)$ are absent because of the form of the actions and currents that are used. Above, we introduced the scales $\Lambda_\chi = 4\pi f_\pi$ with $f_\pi = 132$ MeV and $\Lambda_{\text{QCD}} = 300$ MeV to make all parameters dimensionless. We evaluate a^2q^2 and z using the lattice QCD results for the hadron masses from each individual data set, taking into account their uncertainties and correlations. We evaluate the pole factor in Eq. (36) as

$$\frac{1}{1 - (a^2q^2)/(am_{B_s} + a\Delta^f)^2}, \tag{37}$$

where am_{B_s} are the individual lattice QCD results for the pseudoscalar B_s mass, and $\Delta^f = m^f_{\text{pole}} - m_{B_s,\text{phys}}$ with m^f_{pole} given in Table III and $m_{B_s,\text{phys}} = 5.367$ GeV. In this way, the explicit values of the lattice spacing are needed only for the small term $a\Delta^f$, minimizing the resulting uncertainty. We implement the constraints (7) and (8) at $q^2 = q^2_{\text{max}}$ (corresponding to $z = 0$) by using shared parameters $a^{g_\perp,g_+}_0$, $c^{g_\perp,g_+}_0$, $c^{g_\perp,g_+}_{0,s}$ and $a^{\widetilde{h}_\perp,\widetilde{h}_+}_0$, $c^{\widetilde{h}_\perp,\widetilde{h}_+}_0$, $c^{\widetilde{h}_\perp,\widetilde{h}_+}_{0,s}$ for the form factors $g_\perp$, g_+ and $\widetilde{h}_\perp$, $\widetilde{h}_+$, respectively. The constraints (5) and (6) at $q^2 = 0$ are included using Gaussian priors with widths equal to $z(0)^2$ to allow for the missing higher-order terms in the z expansion.

We refer to the fit using Eq. (36) as the "nominal" fit. In the physical limit $a = 0$, $m_\pi = m_{\pi,\text{phys}}$, $m_{\eta_s} = m_{\eta_s,\text{phys}}$, these functions reduce to the simple form

$$f(q^2) = \frac{1}{1 - q^2/(m^f_{\text{pole}})^2} \left[a^f_0 + a^f_1\, z(q^2)\right]. \tag{38}$$

The values and uncertainties of the parameters a^f_0 and a^f_1 from the nominal fit are given in Table IV; their correlation matrix is given in Tables IX and X. Plots of the lattice data along with the nominal fit functions evaluated in the physical limit are shown in Figs. 3, 4, and 5.

As in Ref. [69], we estimate systematic uncertainties in the extrapolated form factors from the changes in the values and increases in the uncertainties when redoing the fit with added higher-order terms. Here we use the following

f	J^P	$m^f_{\rm pole}$ [GeV]
$f_+,\, f_\perp,\, h_+,\, h_\perp$	1^-	5.416
f_0	0^+	5.711
$g_+,\, g_\perp,\, \widetilde{h}_+,\, \widetilde{h}_\perp$	1^+	5.750
g_0	0^-	5.367

TABLE III. Values of the B_s meson pole masses, $m^f_{\rm pole}$. The 0^- and 1^- masses are from the Particle Data Group [84], while the 0^+ and 1^+ masses were taken from the lattice QCD calculation of Ref. [85]. To evaluate t_+ [defined in Eq. (35)], the values $m_B = 5.279\,\text{GeV}$ and $m_K = 494\,\text{MeV}$ should be used.

functions for the higher-order fit:

$$f_{\rm HO}(q^2) = \frac{1}{1 - q^2/(m^f_{\rm pole})^2}\left[a_0^f\left(1 + c_0^f\frac{m_\pi^2 - m_{\pi,\rm phys}^2}{\Lambda_\chi^2} + \widetilde{c}_0^f\frac{m_\pi^3 - m_{\pi,\rm phys}^3}{\Lambda_\chi^3} + c_{s,0}^f\frac{m_{\eta_s}^2 - m_{\eta_s,\rm phys}^2}{\Lambda_\chi^2} + \widetilde{c}_{s,0}^f\frac{m_{\eta_s}^3 - m_{\eta_s,\rm phys}^3}{\Lambda_\chi^3}\right)\right.$$
$$\left. + a_1^f\left(1 + c_1^f\frac{m_\pi^2 - m_{\pi,\rm phys}^2}{\Lambda_\chi^2} + c_{s,1}^f\frac{m_{\eta_s}^2 - m_{\eta_s,\rm phys}^2}{\Lambda_\chi^2}\right)z(q^2) + a_2^f\,[z(q^2)]^2\right]$$
$$\times\left[1 + b^f\,a^2|\mathbf{p}'|^2 + d^f\,a^2\Lambda_{\rm QCD}^2 + \widetilde{b}^f\,a^4|\mathbf{p}'|^4 + \widehat{d}^f\,a^3\Lambda_{\rm QCD}^3 + \widetilde{d}^f a^4\Lambda_{\rm QCD}^4 + j^f a^4|\mathbf{p}'|^2\Lambda_{\rm QCD}^2\right]. \tag{39}$$

Unlike in Ref. [69], here we do not include terms corresponding to discretization errors proportional to odd powers of $\mathbf{p}'$, as such terms cannot contribute to the ratios used to extract the form factors because of O_h symmetry (we thank Urs Heller for pointing this out). Because the data themselves do not determine the more complex form (39) sufficiently well, we constrain the higher-order coefficients to be natural-sized using Gaussian priors with the following central values and widths:

$$a_2^f = 0 \pm 2\,a_1^f\Big|_{\rm nominal}, \tag{40}$$
$$\widetilde{c}_0^f = 0 \pm 10, \tag{41}$$
$$\widetilde{c}_{s,0}^f = 0 \pm 10, \tag{42}$$
$$c_1^f = 0 \pm 10, \tag{43}$$
$$c_{s,1}^f = 0 \pm 10, \tag{44}$$
$$\widetilde{b}^f = 0 \pm \frac{10}{3^4}, \tag{45}$$
$$\widehat{d}^f = 0 \pm 10, \tag{46}$$
$$\widetilde{d}^f = 0 \pm 10, \tag{47}$$
$$j^f = 0 \pm \frac{10}{3^2}. \tag{48}$$

Here, Eq. (40) means that we set the widths of a_2^f equal to two times the fit results for a_1^f from the nominal fit. In the higher-order fit, we impose the constraints (5) and (6) at $q^2 = 0$ with widths equal to $|z(0)|^3$. The factors of $1/3^n$ for the prior widths of the coefficients of discretization-error terms proportional to $|\mathbf{p}'|^n$ are motivated by the physical picture that the quarks/gluons in the Λ baryon on average carry only some fraction of the momentum $\mathbf{p}'$, estimated to be of order 1/3.

In the higher-order fit, we simultaneously made the following modifications to account for additional sources of systematic uncertainty:

- For the vector and axial vector form factors, in which the residual matching factors in the mostly nonperturbative renormalization procedure and the $\mathcal{O}(a)$-improvement coefficients were computed at one loop, we use bootstrap data for the correlator ratios in which these coefficients were drawn from Gaussian random distributions with central values and widths according to Table III of Ref. [69].

- For the tensor form factors, the renormalization uncertainty is dominated by the use of the tree-level values, $\rho_{T^{\mu\nu}} = 1$, for the residual matching factors in the mostly nonperturbative renormalization procedure. We estimate the systematic uncertainty in $\rho_{T^{\mu\nu}}$ to be equal to 2 times the maximum value of $|\rho_{V^\mu} - 1|$, $|\rho_{A^\mu} - 1|$,

which is equal to 0.05316 [69]. This estimate is larger than one-loop results for $|\rho_{T^{\mu\nu}} - 1|$ obtained in Ref. [18] for the case of staggered light quarks at comparable lattice spacings. Note that $\rho_{T^{\mu\nu}}$ for the tensor current is scale-dependent, and our estimate of the matching uncertainty (and the values of the form factors themselves) should be interpreted as corresponding to $\mu = 4.2$ GeV. To incorporate the tensor-current matching uncertainty in the fit, we introduced nuisance parameters multiplying the tensor form factors, with Gaussian priors equal to 1 ± 0.05316.

- To propagate the uncertainties in the lattice spacings, lattice pion masses, and lattice η_s masses, we promoted these precisely determined quantities to parameters in the fit, with Gaussian priors chosen according to their respective central values and uncertainties.

- We estimate the systematic uncertainties in the form factors resulting from the neglected $d - u$ quark-mass difference and QED to be of order $\mathcal{O}((m_d - m_u)/\Lambda_{\rm QCD}) \approx 0.5\%$ and $\mathcal{O}(\alpha_{\rm e.m.}) \approx 0.7\%$. The systematic uncertainty in the $\Lambda_b \to \Lambda$ form factors due to finite-volume effects is expected to be larger than for $\Lambda_b \to \Lambda_c$ (estimated to be 1.5% in Ref. [69]) but smaller than for $\Lambda_b \to p$ (estimated to be 3% in Ref. [69]), so we take this uncertainty to be 2% here. The systematic uncertainty resulting from the tuning of the relativistic heavy-quark (RHQ) action for the b quark is estimated to be 1% as in Ref. [69], based on the analysis of $B \to \pi$ form factors using the same b-quark action and parameters in Ref. [68]. To incorporate all of these sources of uncertainties in the higher-order fit, we added them to the data correlation matrix used in the fit, treating them as 100% correlated within each of the following groups of form factors: $(f_+, f_\perp, f_0)$, $(g_+, g_\perp, g_0)$, $(h_+, h_\perp)$, and $(\widetilde{h}_+, \widetilde{h}_\perp)$.

In the physical limit $a = 0$, $m_\pi = m_{\pi,\rm phys}$, $m_{\eta_s} = m_{\eta_s,\rm phys}$, the higher-order fit functions reduce to

$$f(q^2) = \frac{1}{1 - q^2/(m^f_{\rm pole})^2}\left[a^f_0 + a^f_1\, z(q^2) + a^f_2\, [z(q^2)]^2\right]. \tag{49}$$

The values and uncertainties of the parameters a^f_0, a^f_1, and a^f_2 from the higher-order fit are given in Table V; their correlation matrix is given in Tables XI and XII. As in Ref. [69], the recommended procedure for computing the central value, statistical uncertainty, and total systematic uncertainty of any observable depending on the form factors is the following:

1. Compute the observable and its uncertainty using the nominal form factors given by Eq. (38), with the parameter values and correlation matrices from Tables IV, IX, and X. Denote the so-obtained central value and uncertainty as

$$O,\ \ \sigma_O. \tag{50}$$

2. Compute the same observable and its uncertainty using the higher-order form factors given by Eq. (49), with the parameter values and correlation matrices from Tables V, XI, and XII. Denote the so-obtained central value and uncertainty as

$$O_{\rm HO},\ \ \sigma_{O,\rm HO}. \tag{51}$$

3. The central value, statistical uncertainty, and systematic uncertainty of the observable are then given by

$$O \ \pm\ \sigma_{O,\rm stat} \ \pm\ \sigma_{O,\rm syst} \tag{52}$$

with

$$\sigma_{O,\rm stat} = \sigma_O, \tag{53}$$

$$\sigma_{O,\rm syst} = \max\left(|O_{\rm HO} - O|,\ \sqrt{|\sigma^2_{O,\rm HO} - \sigma^2_O|}\right). \tag{54}$$

To obtain the total uncertainty, the statistical and systematic uncertainties should be added in quadrature,

$$\sigma_{O,\rm tot} = \sqrt{\sigma^2_{O,\rm stat} + \sigma^2_{O,\rm syst}}. \tag{55}$$

More generally, the total *covariance* between two observables O_1 and O_2 can be computed as

$$\mathrm{cov}_{\rm tot}(O_1,\, O_2) = \mathrm{cov}_{\rm HO}(O_1,\, O_2)\, \frac{\sigma_{O_1,\rm tot}}{\sigma_{O_1,\rm HO}}\, \frac{\sigma_{O_2,\rm tot}}{\sigma_{O_2,\rm HO}}. \tag{56}$$

Parameter	Value	Parameter	Value
$a_0^{f_+}$	0.4221 ± 0.0188	$a_1^{g_0}$	-1.0290 ± 0.1614
$a_1^{f_+}$	-1.1386 ± 0.1683	$a_1^{g_\perp}$	-1.1357 ± 0.1911
$a_0^{f_0}$	0.3725 ± 0.0213	$a_0^{h_+}$	0.4960 ± 0.0258
$a_1^{f_0}$	-0.9389 ± 0.2250	$a_1^{h_+}$	-1.1275 ± 0.2537
$a_0^{f_\perp}$	0.5182 ± 0.0251	$a_0^{h_\perp}$	0.3876 ± 0.0172
$a_1^{f_\perp}$	-1.3495 ± 0.2413	$a_1^{h_\perp}$	-0.9623 ± 0.1550
$a_0^{g_\perp, g_+}$	0.3563 ± 0.0142	$a_0^{\tilde{h}_\perp, \tilde{h}_+}$	0.3403 ± 0.0133
$a_1^{g_+}$	-1.0612 ± 0.1678	$a_1^{\tilde{h}_+}$	-0.7697 ± 0.1612
$a_0^{g_0}$	0.4028 ± 0.0182	$a_1^{\tilde{h}_\perp}$	-0.8008 ± 0.1537

TABLE IV. Central values and uncertainties of the nominal form factor parameters. The correlation matrix is provided in Tables IX and X.

Parameter	Value	Parameter	Value
$a_0^{f_+}$	0.4229 ± 0.0274	$a_2^{g_0}$	1.1490 ± 1.0327
$a_1^{f_+}$	-1.3728 ± 0.3068	$a_1^{g_\perp}$	-1.3607 ± 0.2949
$a_2^{f_+}$	1.7972 ± 1.1506	$a_2^{g_\perp}$	2.4621 ± 1.3711
$a_0^{f_0}$	0.3604 ± 0.0277	$a_0^{h_+}$	0.4753 ± 0.0423
$a_1^{f_0}$	-0.9248 ± 0.3453	$a_1^{h_+}$	-0.8840 ± 0.3997
$a_2^{f_0}$	0.9861 ± 1.1988	$a_2^{h_+}$	-0.8190 ± 1.6760
$a_0^{f_\perp}$	0.5148 ± 0.0353	$a_0^{h_\perp}$	0.3745 ± 0.0313
$a_1^{f_\perp}$	-1.4781 ± 0.4030	$a_1^{h_\perp}$	-0.9439 ± 0.2766
$a_2^{f_\perp}$	1.2496 ± 1.6396	$a_2^{h_\perp}$	1.1606 ± 1.0757
$a_0^{g_\perp, g_+}$	0.3522 ± 0.0205	$a_0^{\tilde{h}_\perp, \tilde{h}_+}$	0.3256 ± 0.0248
$a_1^{g_+}$	-1.2968 ± 0.2732	$a_1^{\tilde{h}_+}$	-0.9603 ± 0.2303
$a_2^{g_+}$	2.7106 ± 1.0665	$a_2^{\tilde{h}_+}$	2.9780 ± 1.0041
$a_0^{g_0}$	0.4059 ± 0.0267	$a_1^{\tilde{h}_\perp}$	-0.9634 ± 0.2268
$a_1^{g_0}$	-1.1622 ± 0.2929	$a_2^{\tilde{h}_\perp}$	2.4782 ± 0.9549

TABLE V. Central values and uncertainties of the higher-order form factor parameters. The correlation matrix is provided in Tables XI and XII.

Plots of the form factors including the total uncertainties are given in Fig. 7. Additionally, Fig. 7 shows estimates of the individual sources of the systematic uncertainties in the form factors, obtained by performing additional fits where each one of the above modifications to the fit functions or data correlation matrix was done individually. We stress that these plots are for illustration only, and the correct procedure for obtaining the total systematic uncertainty in a correlated way is from the full higher-order fit, in which all modifications were done simultaneously.

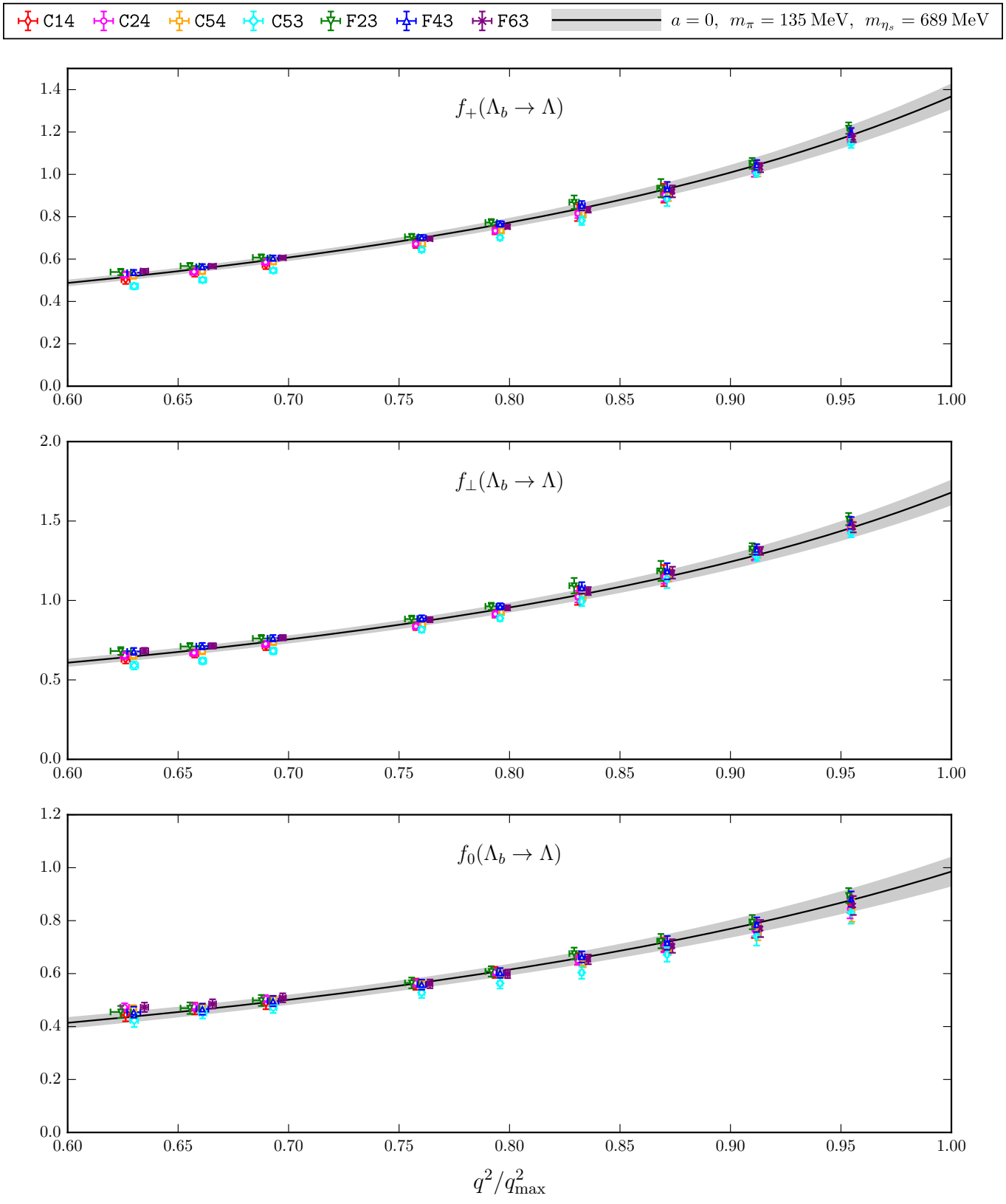

FIG. 3. Vector form factors in the high-q^2 region: lattice results and nominal fit function in the physical limit. The bands indicate the statistical uncertainty.

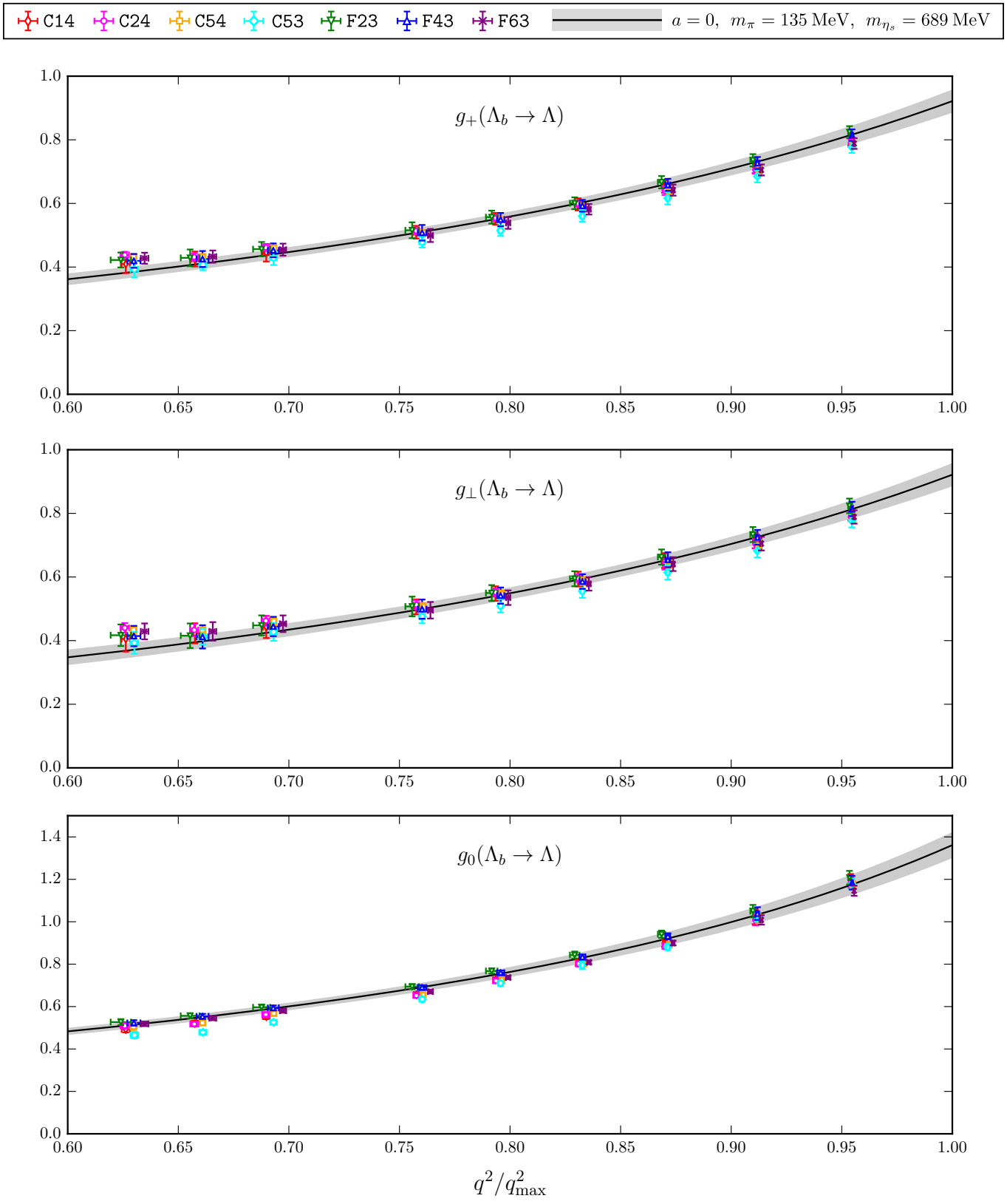

FIG. 4. Axial vector form factors in the high-q^2 region: lattice results and nominal fit function in the physical limit. The bands indicate the statistical uncertainty.

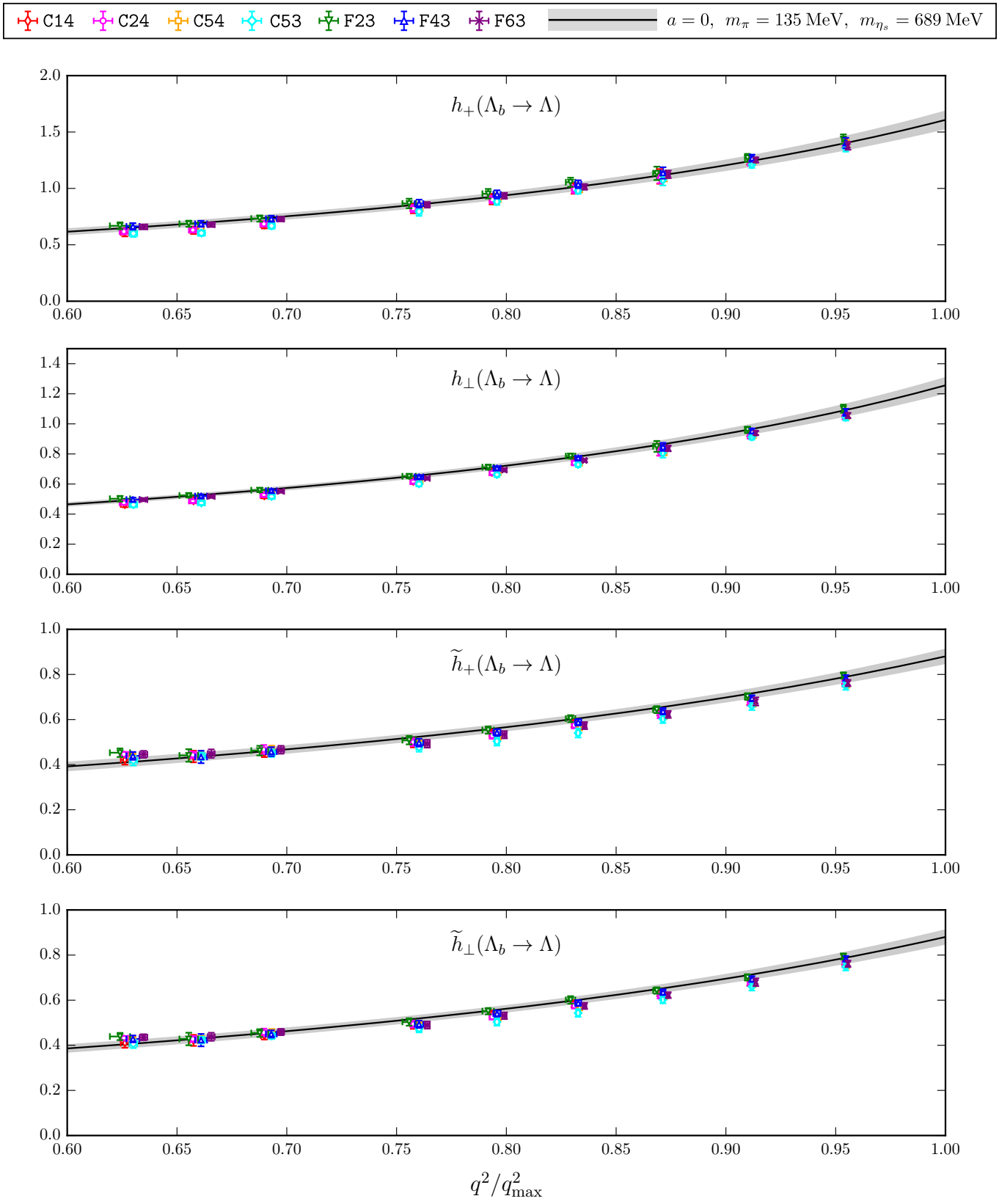

FIG. 5. Tensor form factors in the high-q^2 region: lattice results and nominal fit function in the physical limit. The bands indicate the statistical uncertainty.

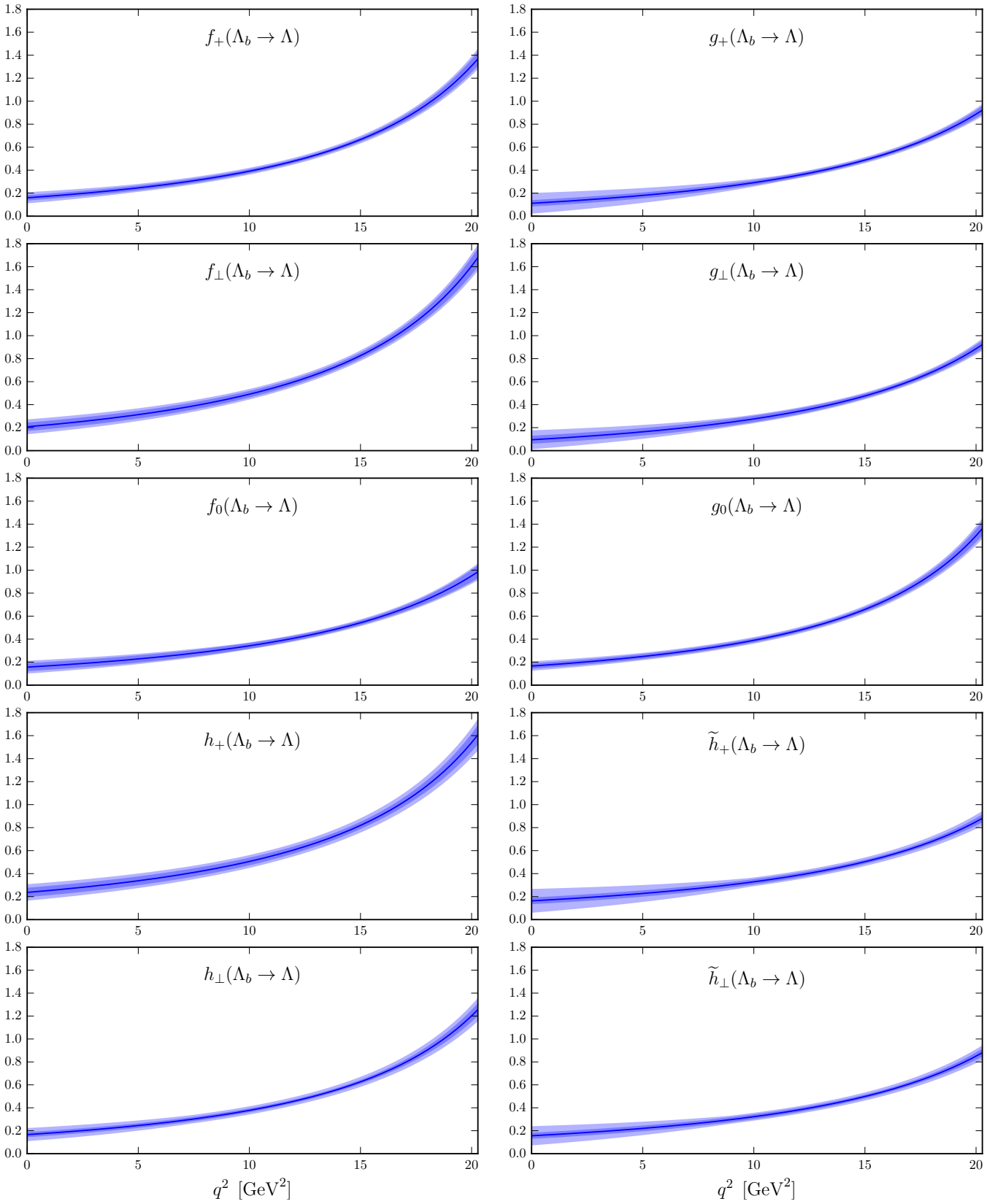

FIG. 6. Form factors in the physical limit, shown over the entire kinematic range. The inner bands show the statistical uncertainty and the outer bands show the total uncertainty.

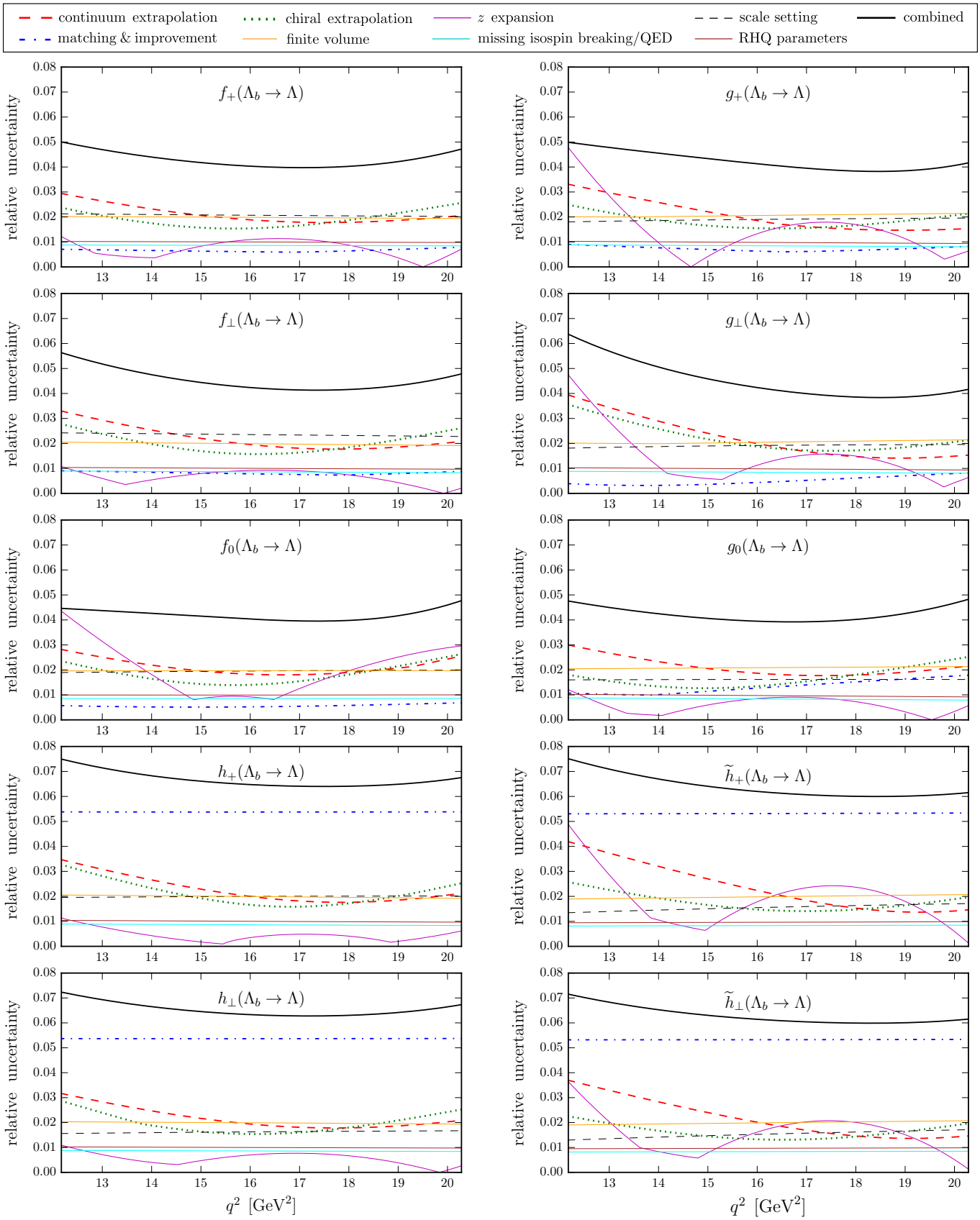

FIG. 7. Systematic uncertainties in the form factors in the high-q^2 region. As explained in the main text and in Ref. [69], the combined uncertainty is not simply the quadratic sum of the individual uncertainties.

V. CALCULATION OF $\Lambda_b \to \Lambda(\to p^+\pi^-)\,\mu^+\mu^-$ OBSERVABLES IN THE STANDARD MODEL

The four-fold differential rate of the decay $\Lambda_b \to \Lambda(\to p^+\pi^-)\,\ell^+\ell^-$ with unpolarized Λ_b can be written as [29, 30]

$$\begin{aligned}\frac{\mathrm{d}^4\Gamma}{\mathrm{d}q^2\,\mathrm{d}\cos\theta_\ell\,\mathrm{d}\cos\theta_\Lambda\,\mathrm{d}\phi} = \frac{3}{8\pi}\Big[&\left(K_{1ss}\sin^2\theta_\ell + K_{1cc}\cos^2\theta_\ell + K_{1c}\cos\theta_\ell\right)\\ &+\left(K_{2ss}\sin^2\theta_\ell + K_{2cc}\cos^2\theta_\ell + K_{2c}\cos\theta_\ell\right)\cos\theta_\Lambda\\ &+\left(K_{3sc}\sin\theta_\ell\cos\theta_\ell + K_{3s}\sin\theta_\ell\right)\sin\theta_\Lambda\sin\phi\\ &+\left(K_{4sc}\sin\theta_\ell\cos\theta_\ell + K_{4s}\sin\theta_\ell\right)\sin\theta_\Lambda\cos\phi\Big],\end{aligned} \tag{57}$$

where the angles θ_l and θ_Λ describe the polar directions of the negatively charged lepton and the proton, respectively, ϕ is the azimuthal angle between the $\ell^+\ell^-$ and $p^+\pi^-$ decay planes, and the coefficients K_i are functions of q^2. The integral of Eq. (57) over the angles gives the q^2-differential decay rate,

$$\frac{\mathrm{d}\Gamma}{\mathrm{d}q^2} = 2K_{1ss} + K_{1cc}. \tag{58}$$

We also define the normalized angular observables

$$\hat{K}_i = \frac{K_i}{\mathrm{d}\Gamma/\mathrm{d}q^2}, \tag{59}$$

of which the combinations

$$F_L = 2\hat{K}_{1ss} - \hat{K}_{1cc}, \tag{60}$$

$$A_{\mathrm{FB}}^{\ell} = \frac{3}{2}\hat{K}_{1c}, \tag{61}$$

$$A_{\mathrm{FB}}^{\Lambda} = \hat{K}_{2ss} + \frac{1}{2}\hat{K}_{2cc}, \tag{62}$$

$$A_{\mathrm{FB}}^{\ell\Lambda} = \frac{3}{4}\hat{K}_{2c} \tag{63}$$

correspond to the fraction of longitudinally polarized dileptons, the lepton-side forward-backward asymmetry, the hadron-side forward-backward asymmetry, and a combined lepton-hadron forward-backward asymmetry [30].

In the approximation where all nonlocal hadronic matrix elements are absorbed via the "effective Wilson coefficients" $C_7^{\mathrm{eff}}(q^2)$ and $C_9^{\mathrm{eff}}(q^2)$, the hadronic contributions to the functions K_i are given by the $\Lambda_b \to \Lambda$ form factors computed here and the $\Lambda \to p^+\pi^-$ decay asymmetry parameter, which is known from experiment to be [84]

$$\alpha_\Lambda = 0.642 \pm 0.013. \tag{64}$$

The expressions for K_i in this approximation are given in Ref. [30] for the case $m_\ell = 0$, and can be obtained for $m_\ell \neq 0$ from Eqs. (A1) and (A2) of Ref. [29]. In the following we focus on the case $\ell = \mu$, which is the most accessible mode at hadron colliders [26–28]. Even though lepton-mass effects are not important for $\ell = \mu$ in most of the kinematic range, we include them here.

Following Ref. [8], we set the effective Wilson coefficients to

$$C_7^{\mathrm{eff}}(q^2) = C_7 - \frac{1}{3}\left[C_3 + \frac{4}{3}C_4 + 20\,C_5 + \frac{80}{3}C_6\right] - \frac{\alpha_s}{4\pi}\left[(C_1 - 6\,C_2)\,F_{1,c}^{(7)}(q^2) + C_8\,F_8^{(7)}(q^2)\right], \tag{65}$$

$$\begin{aligned}C_9^{\mathrm{eff}}(q^2) = {} & C_9 + \frac{4}{3}C_3 + \frac{64}{9}C_5 + \frac{64}{27}C_6 + h(0,q^2)\left(-\frac{1}{2}C_3 - \frac{2}{3}C_4 - 8\,C_5 - \frac{32}{3}C_6\right)\\ & + h(m_b,q^2)\left(-\frac{7}{2}C_3 - \frac{2}{3}C_4 - 38\,C_5 - \frac{32}{3}C_6\right) + h(m_c,q^2)\left(\frac{4}{3}C_1 + C_2 + 6\,C_3 + 60\,C_5\right)\\ & - \frac{\alpha_s}{4\pi}\left[C_1\,F_{1,c}^{(9)}(q^2) + C_2\,F_{2,c}^{(9)}(q^2) + C_8\,F_8^{(9)}(q^2)\right],\end{aligned} \tag{66}$$

where the functions $h(m_q,q^2)$ and $F_8^{(7,9)}(q^2)$ are defined in Eqs. (11), (82), (83) of Ref. [21], and the functions $F_{1,c}^{(7,9)}(q^2)$ and $F_{2,c}^{(7,9)}(q^2)$ are evaluated using the Mathematica packages for high q^2 and low q^2 provided in Ref. [86]

	$\mu = 2.1$ GeV	$\mu = 4.2$ GeV	$\mu = 8.4$ GeV
C_1	−0.4965	−0.2877	−0.1488
C_2	1.0246	1.0101	1.0036
C_3	−0.0143	−0.0060	−0.0027
C_4	−0.1500	−0.0860	−0.0543
C_5	0.0010	0.0004	0.0002
C_6	0.0032	0.0011	0.0004
C_7	−0.3782	−0.3361	−0.3036
C_8	−0.2133	−0.1821	−0.1629
C_9	4.5692	4.2745	3.8698
C_{10}	−4.1602	−4.1602	−4.1602
$m_b^{\overline{\rm MS}}$ [GeV]	4.9236	4.2000	3.7504
α_s	0.2945	0.2233	0.1851
α_e	1/134.44	1/133.28	1/132.51

TABLE VI. Wilson coefficients, b-quark mass, and strong and electromagnetic couplings in the $\overline{\rm MS}$ scheme at the nominal scale $\mu = 4.2\,\text{GeV}$ and at the low and high scales used to estimate the perturbative uncertainties. The values shown here were computed using the `EOS` [92, 93] and `alphaQED` [95, 96] packages. Even though some of the quantities in this table are strongly scale-dependent, most of this dependence cancels in the physical observables.

(the low-q^2 versions are based on Ref. [87]). The effective Wilson coefficients $C_7^{\rm eff}(q^2)$ and $C_9^{\rm eff}(q^2)$ incorporate the leading contributions from an operator product expansion (OPE) of the nonlocal product of $O_{1,\ldots,6;8}$ with the quark electromagnetic current [19, 20]. Unlike in Ref. [19], we have not expanded the functions $h(m_c, q^2)$ and $F_{i,c}^{(7,9)}(q^2)$ in powers of m_c^2/q^2. The subleading contributions from the OPE arise from dimension-5 operators [20], whose matrix elements in the high-q^2 region are suppressed by $\Lambda_{\rm had}^2/Q^2 \sim 1\%$, where $Q^2 \sim \{q^2, m_b^2\}$. Nonfactorizable spectator-scattering effects that are expected to be relevant at low q^2 [21, 62] have not yet been derived for the baryonic decay, and we neglect them here.

We evaluated the Wilson coefficients C_1-C_{10} in the $\overline{\rm MS}$ scheme at next-to-next-to-leading-logarithmic order [88–91] using the `EOS` software [92, 93]; their values are listed in Table VI. The charm and bottom masses appearing in the functions $h(m_q, q^2)$, $F_{1,c}^{(7,9)}(q^2)$, and $F_{2,c}^{(7,9)}(q^2)$ are defined in the pole scheme [86, 87]; we use

$$m_c^{\rm pole} = 1.5953\ \text{GeV}, \tag{67}$$

$$m_b^{\rm pole} = 4.7417\ \text{GeV}, \tag{68}$$

also evaluated with `EOS`. The values of $m_b^{\overline{\rm MS}}$ (which multiplies the operator O_7), α_s, and α_e are given in Table VI. We take the CKM matrix elements from the Summer-2014 Standard-Model fit of the UTFit Collaboration [94],

$$|V_{ts}^* V_{tb}| = 0.04088 \pm 0.00055, \tag{69}$$

and use the Λ_b lifetime

$$\tau_{\Lambda_b} = (1.466 \pm 0.010)\ \text{ps} \tag{70}$$

from the 2015 update of the Review of Particle Physics [84].

Our results for the $\Lambda_b \to \Lambda\mu^+\mu^-$ differential branching fraction and the $\Lambda_b \to \Lambda(\to p^+\pi^-)\mu^+\mu^-$ angular observables are plotted in Figs. 8 and Figs. 9 as the cyan curves (without binning) and the magenta curves (binned). Where available, experimental data from LHCb [28] are included in the figures. Note that for the angular observables, numerator and denominator are binned separately,

$$\langle \hat{K}_i \rangle_{[q^2_{\rm min},\, q^2_{\rm max}]} = \frac{\displaystyle\int_{q^2_{\rm min}}^{q^2_{\rm max}} K_i \, {\rm d}q^2}{\displaystyle\int_{q^2_{\rm min}}^{q^2_{\rm max}} ({\rm d}\Gamma/{\rm d}q^2) \, {\rm d}q^2}. \tag{71}$$

The binned observables are also listed numerically in Table VII, including two additional wider bins at low and high q^2. The observables $\hat{K}_{3s}$ and $\hat{K}_{3sc}$ are negligibly small in the Standard Model and are not shown here.

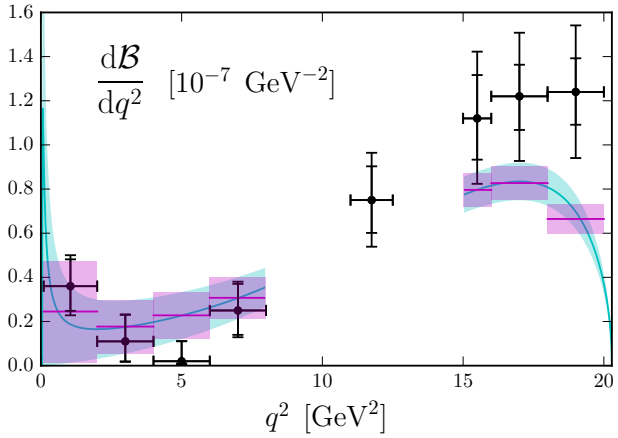

FIG. 8. $\Lambda_b \to \Lambda\,\mu^+\mu^-$ differential branching fraction calculated in the Standard Model, compared to experimental data from LHCb [28] (black points; error bars are shown both including and excluding the uncertainty from the normalization mode $\Lambda_b \to J/\psi\,\Lambda$ [84]).

	$\langle d\mathcal{B}/dq^2\rangle$	$\langle F_L\rangle$	$\langle A_{FB}^{\ell}\rangle$	$\langle A_{FB}^{\Lambda}\rangle$	$\langle A_{FB}^{\ell\Lambda}\rangle$	$\langle \hat{K}_{2ss}\rangle$	$\langle \hat{K}_{2cc}\rangle$	$\langle \hat{K}_{4s}\rangle$	$\langle \hat{K}_{4sc}\rangle$
$[0.1, 2]$	0.25(23)	0.465(84)	0.095(15)	−0.310(18)	−0.0302(51)	−0.233(19)	−0.154(26)	−0.009(22)	0.022(22)
$[2, 4]$	0.18(12)	0.848(27)	0.057(31)	−0.306(24)	−0.0169(99)	−0.284(23)	−0.0444(87)	0.031(36)	0.013(31)
$[4, 6]$	0.23(11)	0.808(42)	−0.062(39)	−0.311(17)	0.021(13)	−0.282(15)	−0.059(13)	0.038(44)	0.001(31)
$[6, 8]$	0.307(94)	0.727(48)	−0.163(40)	−0.316(11)	0.053(13)	−0.273(10)	−0.086(15)	0.030(39)	−0.007(27)
$[1.1, 6]$	0.20(12)	0.813(32)	0.012(31)	−0.309(21)	−0.0027(99)	−0.280(20)	−0.056(10)	0.030(35)	0.009(30)
$[15, 16]$	0.796(75)	0.454(20)	−0.374(14)	−0.3069(83)	0.1286(55)	−0.2253(69)	−0.1633(69)	−0.060(13)	−0.0211(80)
$[16, 18]$	0.827(76)	0.417(15)	−0.372(13)	−0.2891(90)	0.1377(46)	−0.2080(69)	−0.1621(66)	−0.090(10)	−0.0209(60)
$[18, 20]$	0.665(68)	0.3706(79)	−0.309(15)	−0.227(10)	0.1492(37)	−0.1598(71)	−0.1344(70)	−0.1457(74)	−0.0172(40)
$[15, 20]$	0.756(70)	0.409(13)	−0.350(13)	−0.2710(92)	0.1398(43)	−0.1947(68)	−0.1526(65)	−0.1031(97)	−0.0196(55)

TABLE VII. Standard-Model predictions for the binned $\Lambda_b \to \Lambda\,\mu^+\mu^-$ differential branching fraction (in units of 10^{-7} GeV^{-2}) and for the binned $\Lambda_b \to \Lambda(\to p^+\pi^-)\mu^+\mu^-$ angular observables (with unpolarized Λ_b). The first column specifies the bin ranges $[q^2_{\text{min}},\ q^2_{\text{max}}]$ in units of GeV^2.

The uncertainties given for the Standard-Model predictions are the total uncertainties, which include the statistical and systematic uncertainties from the form factors (propagated to the observables using the procedure explained in Sec. IV), the perturbative uncertainties, an estimate of quark-hadron duality violations (discussed further below), and the parametric uncertainties from Eqs. (64), (69), and (70). For all observables considered here (but not for $\hat{K}_{3s}$ and $\hat{K}_{3sc}$), the uncertainties associated with the subleading contributions from the OPE (at high q^2) are negligible compared to the other uncertainties. The central values of the observables were computed at the renormalization scale $\mu = 4.2$ GeV; to estimate the perturbative uncertainties, we varied the renormalization scale from $\mu = 2.1$ GeV to $\mu = 8.4$ GeV. When doing this scale variation, we also included the renormalization-group running of the tensor form factors from the nominal scale $\mu_0 = 4.2$ GeV to the scale μ, by multiplying these form factors with

$$\left(\frac{\alpha_s(\mu)}{\alpha_s(\mu_0)}\right)^{-\gamma_T^{(0)}/(2\beta_0)} \tag{72}$$

(as in Ref. [8]), where $\gamma_T^{(0)} = 2\,C_F = 8/3$ is the anomalous dimension of the tensor current [97], and $\beta_0 = (11\,N_c - 2\,N_f)/3 = 23/3$ is the leading-order QCD beta function [98] for 5 active flavors. Even though we did not perform a one-loop calculation of the residual lattice-to-continuum matching factors for the tensor currents, our estimates of the renormalization uncertainties in the tensor form factors as discussed in Sec. IV are specific for $\mu = 4.2$ GeV, and doing the RG running avoids a double-counting of these uncertainties. Note that the contributions of the tensor form factors to the observables are proportional to $1/q^2$ (because of the photon propagator connecting O_7 to the lepton current), and are suppressed relative to those from the vector and axial vector form factors at high q^2. At low q^2,

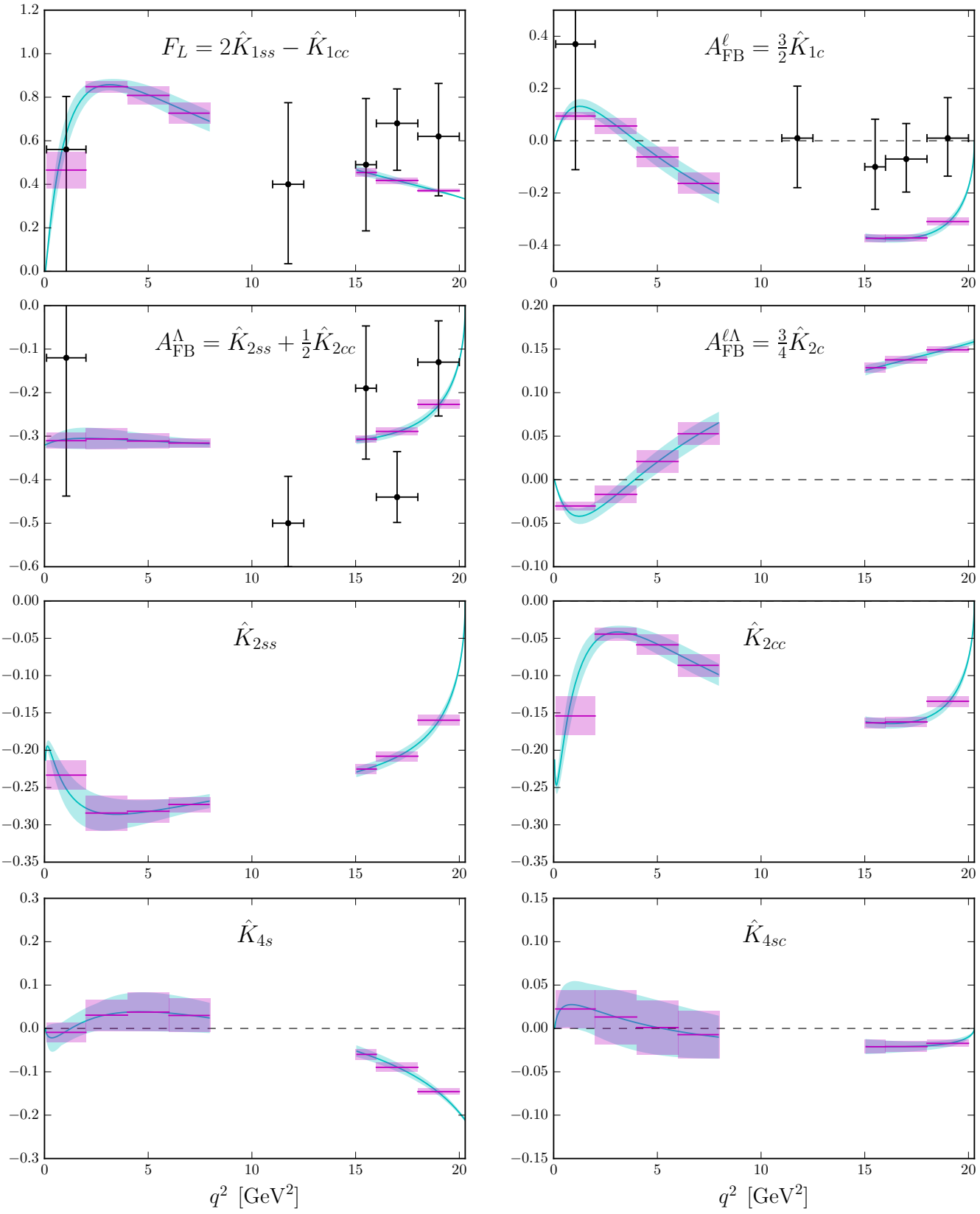

FIG. 9. $\Lambda_b \to \Lambda(\to p^+\pi^-)\mu^+\mu^-$ angular observables calculated in the Standard Model (for unpolarized Λ_b), compared to experimental data from LHCb, where available [28] (black points). The observables $\hat{K}_{3s}$ and $\hat{K}_{3sc}$ are negligibly small in the Standard Model and are therefore not shown here.

the other uncertainties (statistical uncertainties, z-expansion uncertainties, etc.) in the tensor form factors dominate over the uncertainties from the matching factors.

The functions $C_7^{\rm eff}(q^2)$ and $C_9^{\rm eff}(q^2)$ have been computed in perturbation theory and do not correctly describe the local q^2-dependence resulting from charmonium resonances [24]. The q^2-region near $q^2 = m^2_{J/\psi}$ and $q^2 = m^2_{\psi'}$ resonances is excluded for this reason. In the high-q^2 region, which is affected by multiple broad charmonium resonances [24], it is has been argued using quark-hadron duality that these functions correctly describe the charm effects to some extent for observables binned over a wide enough range [20]. The duality violations in the $B \to K\ell^+\ell^-$ decay rate integrated over the high-q^2 region have been estimated in Ref. [20] to be of order 2%. We instead include an overall 5% uncertainty on both $C_7^{\rm eff}(q^2)$ and $C_9^{\rm eff}(q^2)$ to account for these effects, which increases the uncertainty in the $\Lambda_b \to \Lambda\ell^+\ell^-$ decay rate at high q^2 by approximately 5%. We use the same 5% uncertainty on $C_7^{\rm eff}(q^2)$ and $C_9^{\rm eff}(q^2)$ at low q^2, even though there is no good theoretical basis for it. We are unable to estimate the uncertainties resulting from the neglected spectator-scattering effects at low q^2, but it is likely that these uncertainties are smaller than the large form factor uncertainties in that region, at least for the differential branching fraction.

In our calculation of the $\Lambda_b \to \Lambda(\to p^+\pi^-)\mu^+\mu^-$ angular observables, we have treated the Λ_b's as unpolarized. The polarization vector of Λ_b baryons produced through the strong interaction is expected to be perpendicular to the production plane spanned by the Λ_b momentum and the beam direction, as a consequence of parity conservation [99]. Taking into account this polarization direction, the $\Lambda_b \to \Lambda(\to p^+\pi^-)\mu^+\mu^-$ angular distribution then becomes dependent on five angles [49], as illustrated in Fig. 1 of Ref. [48] for the similar decay $\Lambda_b \to \Lambda(\to p^+\pi^-)J/\psi(\to \mu^+\mu^-)$. For a particle detector with isotropic acceptance, the polarization effects will average out if the additional angles are not reconstructed. This is not the case for the asymmetric LHCb detector [100], but the polarization parameter for Λ_b baryons produced at the LHC was measured to be small and consistent with zero, $P_b = 0.06 \pm 0.07 \pm 0.02$ (at $\sqrt{s} = 7$ TeV) [48]. The resulting effects are therefore expected to be small. Because the polarization effects depend on the details of the detector and on the experimental analysis, their study is beyond the scope of the present work.

VI. DISCUSSION

The baryonic decay $\Lambda_b \to \Lambda(\to p^+\pi^-)\mu^+\mu^-$ can provide valuable new information on the physics of the $b \to s\mu^+\mu^-$ transition, and hence on possible physics beyond the Standard Model. Here we have presented a high-precision lattice QCD calculation of the relevant $\Lambda_b \to \Lambda$ form factors. Using a relativistic heavy-quark action, we have computed the ten helicity form factors describing the $\Lambda_b \to \Lambda$ matrix elements of the $b \to s$ vector, axial vector, and tensor currents directly at the physical b-quark mass. Compared to Ref. [15], where we treated the b quark in the static limit, this work significantly reduces the theoretical uncertainties in the form factors and hence in phenomenological applications. As in Ref. [69], we provide the form factors in terms of two sets of z-expansion parameters. The "nominal" parameters and their correlation matrix are given in Tables IV, IX, X, and are used to compute the central values and statistical uncertainties. The "higher-order" parameters and their correlation matrix are given in Tables V, XI, XII, and are used in combination with the nominal parameters to compute the systematic uncertainties in a fully correlated way. Data files containing all form factor parameters and their covariance matrices are also available as supplemental material. Plots of the form factors with error bands indicating the total uncertainties are shown in Fig. 6. Our results for all ten form factors are consistent with those of the recent QCD light-cone sum-rule calculation [62], and our uncertainties are much smaller in most of the kinematic range.

Standard-Model predictions for the $\Lambda_b \to \Lambda(\to p^+\pi^-)\mu^+\mu^-$ differential branching fraction and angular observables using our form factor results are presented in Figs. 8, 9 and Table VII. In Table VIII below, we show a further comparison with LHCb results [28] in the bin $[15\,\text{GeV}^2, 20\,\text{GeV}^2]$, where both our predictions and the experimental data are most precise.

	This work	LHCb
$\langle d\mathcal{B}/dq^2\rangle_{[15,\,20]}$	0.756 ± 0.070	1.20 ± 0.27
$\langle F_L\rangle_{[15,\,20]}$	0.409 ± 0.013	$0.61^{+0.11}_{-0.14}$
$\langle A_{\rm FB}^{\ell}\rangle_{[15,\,20]}$	-0.350 ± 0.013	-0.05 ± 0.09
$\langle A_{\rm FB}^{\Lambda}\rangle_{[15,\,20]}$	-0.2710 ± 0.0092	-0.29 ± 0.08

TABLE VIII. Comparison of our results for the $\Lambda_b \to \Lambda(\to p^+\pi^-)\mu^+\mu^-$ observables with LHCb data [28] in the bin $[15\,\text{GeV}^2, 20\,\text{GeV}^2]$.

In this bin, the magnitude of the lepton-side forward-backward asymmetry measured by LHCb is smaller than the theoretical value by 3.3σ. The measured differential branching fraction exceeds the theoretical value by 1.6σ.

While the latter deviation is not yet statistically significant, it is in the opposite direction to what has been observed for the decays $B \to K^{(*)}\mu^+\mu^-$ and $B_s \to \phi\mu^+\mu^-$ [5–11]. A negative shift in the Wilson coefficient C_9 alone, the simplest scenario that significantly improves the agreement between theory and experiment in global fits of mesonic observables [2, 13, 14], would further lower the predicted $\Lambda_b \to \Lambda\,\mu^+\mu^-$ differential branching fraction. It is possible that the tensions are caused by the broad charmonium resonances in this kinematic region [24], which may contribute to the baryonic decay rate with the opposite sign. This would correspond to duality violations in the operator product expansion used here to treat the nonlocal matrix elements of O_1 and O_2 that are much larger than estimated previously [20]. More precise experimental results, including for the branching ratio of the normalization mode $\Lambda_b \to J/\psi\,\Lambda$, would be very useful in clarifying this aspect of the results.

ACKNOWLEDGMENTS

SM would like to thank Danny van Dyk for discussions. We are grateful to the RBC and UKQCD collaborations for making their gauge field configurations available. The lattice calculations were carried out using the Chroma software [101] on high-performance computing resources provided by XSEDE (supported by National Science Foundation Grant Number OCI-1053575) and NERSC (supported by U.S. Department of Energy Grant Number DE-AC02-05CH11231). SM is supported by National Science Foundation Grant Number PHY-1520996, and by the RHIC Physics Fellow Program of the RIKEN BNL Research Center. WD was partially supported by the U.S. Department of Energy Early Career Research Award DE-SC0010495 and under Grant No. DE-SC0011090.

Appendix A: Additional tables

	$a_0^{f_+}$	$a_1^{f_+}$	$a_0^{f_0}$	$a_1^{f_0}$	$a_0^{f_\perp}$	$a_1^{f_\perp}$	$a_0^{g_\perp,g_+}$	$a_1^{g_+}$	$a_0^{g_0}$
$a_0^{f_+}$	1	−0.8899	0.5529	−0.4746	0.7636	−0.5961	0.6314	−0.4590	0.7879
$a_1^{f_+}$	−0.8899	1	−0.5184	0.5200	−0.6740	0.6363	−0.5654	0.4889	−0.6672
$a_0^{f_0}$	0.5529	−0.5184	1	−0.8684	0.4563	−0.3557	0.6190	−0.4499	0.5184
$a_1^{f_0}$	−0.4746	0.5200	−0.8684	1	−0.3870	0.3385	−0.5356	0.5178	−0.4440
$a_0^{f_\perp}$	0.7636	−0.6740	0.4563	−0.3870	1	−0.8522	0.5521	−0.4026	0.7538
$a_1^{f_\perp}$	−0.5961	0.6363	−0.3557	0.3385	−0.8522	1	−0.4408	0.3880	−0.5619
$a_0^{g_\perp,g_+}$	0.6314	−0.5654	0.6190	−0.5356	0.5521	−0.4408	1	−0.8228	0.6553
$a_1^{g_+}$	−0.4590	0.4889	−0.4499	0.5178	−0.4026	0.3880	−0.8228	1	−0.4987
$a_0^{g_0}$	0.7879	−0.6672	0.5184	−0.4440	0.7538	−0.5619	0.6553	−0.4987	1
$a_1^{g_0}$	−0.6552	0.6780	−0.4417	0.4364	−0.6481	0.6409	−0.5819	0.5587	−0.8668
$a_1^{g_\perp}$	−0.4118	0.4324	−0.3960	0.4799	−0.3575	0.3304	−0.7533	0.8361	−0.4530
$a_0^{h_+}$	0.7013	−0.6149	0.3954	−0.3347	0.7084	−0.5691	0.4943	−0.3617	0.6995
$a_1^{h_+}$	−0.4922	0.5349	−0.2781	0.2624	−0.5217	0.5722	−0.3669	0.3343	−0.4721
$a_0^{h_\perp}$	0.7958	−0.6896	0.4976	−0.4157	0.7737	−0.6057	0.5981	−0.4331	0.7868
$a_1^{h_\perp}$	−0.6561	0.6714	−0.4222	0.4030	−0.6574	0.6439	−0.5073	0.4432	−0.6300
$a_0^{\tilde{h}_\perp,\tilde{h}_+}$	0.6359	−0.5614	0.6563	−0.5538	0.5483	−0.4313	0.7480	−0.5742	0.6416
$a_1^{\tilde{h}_+}$	−0.3785	0.4062	−0.3576	0.4487	−0.3298	0.3217	−0.4788	0.5313	−0.3976
$a_1^{\tilde{h}_\perp}$	−0.3969	0.4324	−0.3952	0.4721	−0.3445	0.3482	−0.5159	0.5621	−0.4100

TABLE IX. Correlation matrix of the nominal form factor parameters, part 1.

	$a_1^{g_0}$	$a_1^{g_\perp}$	$a_0^{h_+}$	$a_1^{h_+}$	$a_0^{h_\perp}$	$a_1^{h_\perp}$	$a_0^{\tilde{h}_\perp,\tilde{h}_+}$	$a_1^{\tilde{h}_+}$	$a_1^{\tilde{h}_\perp}$
$a_0^{f_+}$	−0.6552	−0.4118	0.7013	−0.4922	0.7958	−0.6561	0.6359	−0.3785	−0.3969
$a_1^{f_+}$	0.6780	0.4324	−0.6149	0.5349	−0.6896	0.6714	−0.5614	0.4062	0.4324
$a_0^{f_0}$	−0.4417	−0.3960	0.3954	−0.2781	0.4976	−0.4222	0.6563	−0.3576	−0.3952
$a_1^{f_0}$	0.4364	0.4799	−0.3347	0.2624	−0.4157	0.4030	−0.5538	0.4487	0.4721
$a_0^{f_\perp}$	−0.6481	−0.3575	0.7084	−0.5217	0.7737	−0.6574	0.5483	−0.3298	−0.3445
$a_1^{f_\perp}$	0.6409	0.3304	−0.5691	0.5722	−0.6057	0.6439	−0.4313	0.3217	0.3482
$a_0^{g_\perp,g_+}$	−0.5819	−0.7533	0.4943	−0.3669	0.5981	−0.5073	0.7480	−0.4788	−0.5159
$a_1^{g_+}$	0.5587	0.8361	−0.3617	0.3343	−0.4331	0.4432	−0.5742	0.5313	0.5621
$a_0^{g_0}$	−0.8668	−0.4530	0.6995	−0.4721	0.7868	−0.6300	0.6416	−0.3976	−0.4100
$a_1^{g_0}$	1	0.4923	−0.5981	0.5503	−0.6558	0.6600	−0.5503	0.4241	0.4542
$a_1^{g_\perp}$	0.4923	1	−0.3233	0.2886	−0.3896	0.3907	−0.5186	0.5070	0.5339
$a_0^{h_+}$	−0.5981	−0.3233	1	−0.8048	0.7363	−0.6286	0.4842	−0.2961	−0.3080
$a_1^{h_+}$	0.5503	0.2886	−0.8048	1	−0.5298	0.5920	−0.3582	0.2782	0.3046
$a_0^{h_\perp}$	−0.6558	−0.3896	0.7363	−0.5298	1	−0.8738	0.5995	−0.3660	−0.3791
$a_1^{h_\perp}$	0.6600	0.3907	−0.6286	0.5920	−0.8738	1	−0.5044	0.3793	0.4023
$a_0^{\tilde{h}_\perp,\tilde{h}_+}$	−0.5503	−0.5186	0.4842	−0.3582	0.5995	−0.5044	1	−0.7185	−0.7634
$a_1^{\tilde{h}_+}$	0.4241	0.5070	−0.2961	0.2782	−0.3660	0.3793	−0.7185	1	0.9448
$a_1^{\tilde{h}_\perp}$	0.4542	0.5339	−0.3080	0.3046	−0.3791	0.4023	−0.7634	0.9448	1

TABLE X. Correlation matrix of the nominal form factor parameters, part 2.

	$a_0^{f_+}$	$a_1^{f_+}$	$a_2^{f_+}$	$a_0^{f_0}$	$a_1^{f_0}$	$a_2^{f_0}$	$a_0^{f_\perp}$	$a_1^{f_\perp}$	$a_2^{f_\perp}$	$a_0^{g_\perp,g_+}$	$a_1^{g_+}$	$a_2^{g_+}$	$a_0^{g_0}$	$a_1^{g_0}$
$a_0^{f_+}$	1	−0.7339	0.2311	0.5619	−0.3171	−0.0104	0.6938	−0.3846	0.0292	0.4710	−0.2594	−0.0054	0.5532	−0.3705
$a_1^{f_+}$	−0.7339	1	−0.6732	−0.3259	0.2406	−0.0108	−0.4352	0.3415	−0.0397	−0.3060	0.2112	0.0169	−0.3805	0.3368
$a_2^{f_+}$	0.2311	−0.6732	1	−0.0709	0.0673	0.2478	0.0784	−0.1001	0.0886	−0.0058	0.0161	0.0399	0.0399	−0.0797
$a_0^{f_0}$	0.5619	−0.3259	−0.0709	1	−0.7563	0.3096	0.4994	−0.2483	−0.0045	0.4748	−0.2686	0.0179	0.4091	−0.2573
$a_1^{f_0}$	−0.3171	0.2406	0.0673	−0.7563	1	−0.7158	−0.2727	0.1794	0.0104	−0.3182	0.2729	−0.0497	−0.2673	0.2101
$a_2^{f_0}$	−0.0104	−0.0108	0.2478	0.3096	−0.7158	1	0.0135	0.0004	0.0417	0.0446	−0.0818	0.1067	0.0086	−0.0129
$a_0^{f_\perp}$	0.6938	−0.4352	0.0784	0.4994	−0.2727	0.0135	1	−0.7106	0.1636	0.4375	−0.2323	−0.0217	0.5475	−0.3836
$a_1^{f_\perp}$	−0.3846	0.3415	−0.1001	−0.2483	0.1794	0.0004	−0.7106	1	−0.5951	−0.2540	0.1760	0.0317	−0.3372	0.3297
$a_2^{f_\perp}$	0.0292	−0.0397	0.0886	−0.0045	0.0104	0.0417	0.1636	−0.5951	1	−0.0062	0.0012	0.0709	0.0097	−0.0288
$a_0^{g_\perp,g_+}$	0.4710	−0.3060	−0.0058	0.4748	−0.3182	0.0446	0.4375	−0.2540	−0.0062	1	−0.6700	0.2588	0.6125	−0.3281
$a_1^{g_+}$	−0.2594	0.2112	0.0161	−0.2686	0.2729	−0.0818	−0.2323	0.1760	0.0012	−0.6700	1	−0.7221	−0.3059	0.2228
$a_2^{g_+}$	−0.0054	0.0169	0.0399	0.0179	−0.0497	0.1067	−0.0217	0.0317	0.0709	0.2588	−0.7221	1	−0.0097	0.0306
$a_0^{g_0}$	0.5532	−0.3805	0.0399	0.4091	−0.2673	0.0086	0.5475	−0.3372	0.0097	0.6125	−0.3059	−0.0097	1	−0.7498
$a_1^{g_0}$	−0.3705	0.3368	−0.0797	−0.2573	0.2101	−0.0129	−0.3836	0.3297	−0.0288	−0.3281	0.2228	0.0306	−0.7498	1
$a_2^{g_0}$	0.0577	−0.0808	0.1347	0.0055	0.0125	0.0479	0.0769	−0.0978	0.1067	−0.0163	0.0246	0.2410	0.3002	−0.6973
$a_1^{g_\perp}$	−0.2617	0.2120	0.0179	−0.2593	0.2696	−0.0805	−0.2358	0.1774	0.0082	−0.6393	0.6447	−0.3001	−0.3186	0.2276
$a_2^{g_\perp}$	0.0270	−0.0266	0.0411	0.0295	−0.0421	0.0621	0.0234	−0.0206	0.0237	0.1673	−0.1942	0.2013	0.0413	−0.0259
$a_0^{h_+}$	0.4320	−0.2957	0.0442	0.2896	−0.1765	−0.0057	0.4519	−0.2842	0.0133	0.3361	−0.1753	−0.0184	0.4208	−0.2903
$a_1^{h_+}$	−0.2916	0.2563	−0.0692	−0.1879	0.1305	0.0104	−0.3212	0.2789	−0.0261	−0.2291	0.1513	0.0285	−0.2745	0.2529
$a_2^{h_+}$	−0.0357	0.0142	0.0352	−0.0462	0.0393	0.0042	−0.0374	0.0073	0.0704	−0.0407	0.0179	0.0451	−0.0417	0.0204
$a_0^{h_\perp}$	0.4485	−0.3123	0.0454	0.3170	−0.2001	0.0013	0.4560	−0.2870	0.0148	0.3552	−0.1921	−0.0113	0.4346	−0.2975
$a_1^{h_\perp}$	−0.3831	0.3277	−0.0854	−0.2633	0.1966	−0.0142	−0.4047	0.3250	−0.0403	−0.2890	0.1881	0.0125	−0.3616	0.3153
$a_2^{h_\perp}$	0.0149	−0.0429	0.0852	−0.0129	0.0074	0.0366	0.0197	−0.0473	0.0898	−0.0164	0.0058	0.0545	0.0112	−0.0390
$a_0^{\tilde{h}_\perp,\tilde{h}_+}$	0.3554	−0.2258	−0.0057	0.3704	−0.2463	0.0401	0.3277	−0.1850	−0.0030	0.4066	−0.2438	0.0268	0.3407	−0.2088
$a_1^{\tilde{h}_+}$	−0.2489	0.1846	0.0063	−0.2451	0.2691	−0.1224	−0.2250	0.1514	0.0006	−0.3005	0.2828	−0.0927	−0.2442	0.1771
$a_2^{\tilde{h}_+}$	−0.0086	0.0188	0.0369	−0.0109	0.0012	0.0578	−0.0160	0.0276	0.0148	−0.0210	0.0074	0.0700	−0.0081	0.0150
$a_1^{\tilde{h}_\perp}$	−0.2546	0.1962	0.0040	−0.2643	0.2785	−0.1175	−0.2284	0.1638	0.0003	−0.3173	0.2952	−0.0894	−0.2437	0.1851
$a_2^{\tilde{h}_\perp}$	−0.0114	0.0174	0.0358	−0.0081	−0.0125	0.0694	−0.0201	0.0250	0.0212	−0.0198	−0.0027	0.0853	−0.0167	0.0204

TABLE XI. Correlation matrix of the higher-order form factor parameters, part 1.

	$a_2^{g_0}$	$a_1^{g_\perp}$	$a_2^{g_\perp}$	$a_0^{h_+}$	$a_1^{h_+}$	$a_2^{h_+}$	$a_0^{h_\perp}$	$a_1^{h_\perp}$	$a_2^{h_\perp}$	$a_0^{\widetilde{h}_\perp,\widetilde{h}_+}$	$a_1^{\widetilde{h}_+}$	$a_2^{\widetilde{h}_+}$	$a_1^{\widetilde{h}_\perp}$	$a_2^{\widetilde{h}_\perp}$
$a_0^{f_+}$	0.0577	−0.2617	0.0270	0.4320	−0.2916	−0.0357	0.4485	−0.3831	0.0149	0.3554	−0.2489	−0.0086	−0.2546	−0.0114
$a_1^{f_+}$	−0.0808	0.2120	−0.0266	−0.2957	0.2563	0.0142	−0.3123	0.3277	−0.0429	−0.2258	0.1846	0.0188	0.1962	0.0174
$a_2^{f_+}$	0.1347	0.0179	0.0411	0.0442	−0.0692	0.0352	0.0454	−0.0854	0.0852	−0.0057	0.0063	0.0369	0.0040	0.0358
$a_0^{f_0}$	0.0055	−0.2593	0.0295	0.2896	−0.1879	−0.0462	0.3170	−0.2633	−0.0129	0.3704	−0.2451	−0.0109	−0.2643	−0.0081
$a_1^{f_0}$	0.0125	0.2696	−0.0421	−0.1765	0.1305	0.0393	−0.2001	0.1966	0.0074	−0.2463	0.2691	0.0012	0.2785	−0.0125
$a_2^{f_0}$	0.0479	−0.0805	0.0621	−0.0057	0.0104	0.0042	0.0013	−0.0142	0.0366	0.0401	−0.1224	0.0578	−0.1175	0.0694
$a_0^{f_\perp}$	0.0769	−0.2358	0.0234	0.4519	−0.3212	−0.0374	0.4560	−0.4047	0.0197	0.3277	−0.2250	−0.0160	−0.2284	−0.0201
$a_1^{f_\perp}$	−0.0978	0.1774	−0.0206	−0.2842	0.2789	0.0073	−0.2870	0.3250	−0.0473	−0.1850	0.1514	0.0276	0.1638	0.0250
$a_2^{f_\perp}$	0.1067	0.0082	0.0237	0.0133	−0.0261	0.0704	0.0148	−0.0403	0.0898	−0.0030	0.0006	0.0148	0.0003	0.0212
$a_0^{g_\perp,g_+}$	−0.0163	−0.6393	0.1673	0.3361	−0.2291	−0.0407	0.3552	−0.2890	−0.0164	0.4066	−0.3005	−0.0210	−0.3173	−0.0198
$a_1^{g_+}$	0.0246	0.6447	−0.1942	−0.1753	0.1513	0.0179	−0.1921	0.1881	0.0058	−0.2438	0.2828	0.0074	0.2952	−0.0027
$a_2^{g_+}$	0.2410	−0.3001	0.2013	−0.0184	0.0285	0.0451	−0.0113	0.0125	0.0545	0.0268	−0.0927	0.0700	−0.0894	0.0853
$a_0^{g_0}$	0.3002	−0.3186	0.0413	0.4208	−0.2745	−0.0417	0.4346	−0.3616	0.0112	0.3407	−0.2442	−0.0081	−0.2437	−0.0167
$a_1^{g_0}$	−0.6973	0.2276	−0.0259	−0.2903	0.2529	0.0204	−0.2975	0.3153	−0.0390	−0.2088	0.1771	0.0150	0.1851	0.0204
$a_2^{g_0}$	1	0.0596	0.0566	0.0557	−0.0566	0.0488	0.0536	−0.0887	0.1011	−0.0066	0.0138	0.0560	0.0153	0.0591
$a_1^{g_\perp}$	0.0596	1	−0.6002	−0.1793	0.1546	0.0228	−0.1944	0.1894	0.0106	−0.2341	0.2793	0.0028	0.2914	−0.0052
$a_2^{g_\perp}$	0.0566	−0.6002	1	0.0130	−0.0169	0.0193	0.0158	−0.0238	0.0271	0.0153	−0.0596	0.0756	−0.0585	0.0801
$a_0^{h_+}$	0.0557	−0.1793	0.0130	1	−0.6176	0.0511	0.7980	−0.4369	0.0429	0.6438	−0.2746	0.0256	−0.2824	0.0178
$a_1^{h_+}$	−0.0566	0.1546	−0.0169	−0.6176	1	−0.5243	−0.3409	0.3166	−0.0457	−0.2502	0.1550	0.0209	0.1710	0.0192
$a_2^{h_+}$	0.0488	0.0228	0.0193	0.0511	−0.5243	1	−0.0408	0.0050	0.0879	−0.0406	0.0261	0.0128	0.0249	0.0180
$a_0^{h_\perp}$	0.0536	−0.1944	0.0158	0.7980	−0.3409	−0.0408	1	−0.6707	0.1528	0.6864	−0.2997	0.0313	−0.3079	0.0255
$a_1^{h_\perp}$	−0.0887	0.1894	−0.0238	−0.4369	0.3166	0.0050	−0.6707	1	−0.5892	−0.3283	0.2053	0.0143	0.2167	0.0099
$a_2^{h_\perp}$	0.1011	0.0106	0.0271	0.0429	−0.0457	0.0879	0.1528	−0.5892	1	0.0151	0.0017	0.0199	0.0001	0.0246
$a_0^{\widetilde{h}_\perp,\widetilde{h}_+}$	−0.0066	−0.2341	0.0153	0.6438	−0.2502	−0.0406	0.6864	−0.3283	0.0151	1	−0.5627	0.1115	−0.5850	0.1175
$a_1^{\widetilde{h}_+}$	0.0138	0.2793	−0.0596	−0.2746	0.1550	0.0261	−0.2997	0.2053	0.0017	−0.5627	1	−0.4627	0.7130	−0.2025
$a_2^{\widetilde{h}_+}$	0.0560	0.0028	0.0756	0.0256	0.0209	0.0128	0.0313	0.0143	0.0199	0.1115	−0.4627	1	−0.1630	0.4328
$a_1^{\widetilde{h}_\perp}$	0.0153	0.2914	−0.0585	−0.2824	0.1710	0.0249	−0.3079	0.2167	0.0001	−0.5850	0.7130	−0.1630	1	−0.5189
$a_2^{\widetilde{h}_\perp}$	0.0591	−0.0052	0.0801	0.0178	0.0192	0.0180	0.0255	0.0099	0.0246	0.1175	−0.2025	0.4328	−0.5189	1

TABLE XII. Correlation matrix of the higher-order form factor parameters, part 2.

	$\|\mathbf{p}'\|^2/(2\pi/L)^2$	C14	C24	C54	C53	F23	F43	F63
f_+	1	1.189(25)	1.174(21)	1.168(22)	1.145(20)	1.218(27)	1.198(21)	1.172(19)
	2	1.024(35)	1.013(23)	1.014(24)	1.006(17)	1.052(25)	1.044(23)	1.032(22)
	3	0.911(44)	0.901(28)	0.902(28)	0.885(34)	0.935(43)	0.930(34)	0.920(28)
	4	0.820(40)	0.816(22)	0.814(19)	0.782(20)	0.868(32)	0.852(22)	0.833(14)
	5	0.737(20)	0.734(13)	0.735(14)	0.701(11)	0.773(16)	0.766(13)	0.7529(98)
	6	0.672(19)	0.672(13)	0.673(13)	0.644(10)	0.705(14)	0.702(12)	0.6960(94)
	8	0.572(19)	0.586(13)	0.588(14)	0.546(11)	0.608(15)	0.604(13)	0.6064(98)
	9	0.537(20)	0.540(14)	0.543(14)	0.501(12)	0.567(15)	0.564(13)	0.567(10)
	10	0.503(20)	0.527(15)	0.522(15)	0.472(14)	0.539(15)	0.536(13)	0.544(10)
$f_\perp$	1	1.479(32)	1.466(28)	1.470(31)	1.424(27)	1.512(38)	1.488(37)	1.461(32)
	2	1.297(41)	1.281(30)	1.297(30)	1.275(25)	1.325(35)	1.321(33)	1.312(25)
	3	1.157(67)	1.148(42)	1.160(40)	1.134(56)	1.186(63)	1.183(51)	1.175(37)
	4	1.030(58)	1.024(36)	1.034(31)	0.994(29)	1.093(49)	1.079(36)	1.059(25)
	5	0.917(25)	0.915(20)	0.927(20)	0.888(18)	0.963(22)	0.962(20)	0.954(16)
	6	0.839(25)	0.838(19)	0.848(20)	0.816(18)	0.883(21)	0.886(20)	0.879(16)
	8	0.712(25)	0.726(20)	0.738(20)	0.682(21)	0.761(22)	0.762(20)	0.766(17)
	9	0.666(25)	0.670(20)	0.681(20)	0.620(20)	0.711(22)	0.712(20)	0.714(17)
	10	0.630(26)	0.654(22)	0.654(22)	0.590(24)	0.682(24)	0.679(22)	0.683(18)
f_0	1	0.863(33)	0.845(36)	0.837(42)	0.830(42)	0.895(28)	0.881(29)	0.857(36)
	2	0.768(34)	0.765(24)	0.756(30)	0.741(35)	0.794(27)	0.785(27)	0.770(32)
	3	0.709(26)	0.699(19)	0.694(23)	0.672(27)	0.723(27)	0.716(26)	0.704(26)
	4	0.656(23)	0.650(16)	0.640(17)	0.604(23)	0.676(23)	0.663(21)	0.654(18)
	5	0.605(21)	0.605(13)	0.599(13)	0.563(20)	0.608(20)	0.602(18)	0.599(16)
	6	0.560(21)	0.564(13)	0.558(13)	0.528(20)	0.565(20)	0.558(19)	0.561(16)
	8	0.488(22)	0.505(13)	0.503(14)	0.471(20)	0.499(21)	0.496(20)	0.508(17)
	9	0.468(22)	0.475(14)	0.474(14)	0.450(20)	0.469(22)	0.465(21)	0.485(17)
	10	0.444(24)	0.473(14)	0.467(14)	0.423(25)	0.455(23)	0.454(21)	0.473(18)
g_+	1	0.802(19)	0.790(12)	0.785(12)	0.777(18)	0.824(19)	0.815(18)	0.788(17)
	2	0.715(20)	0.706(12)	0.701(15)	0.685(19)	0.736(19)	0.727(19)	0.705(17)
	3	0.653(20)	0.641(14)	0.637(16)	0.616(20)	0.667(19)	0.658(19)	0.642(17)
	4	0.597(19)	0.5992(94)	0.5907(91)	0.560(17)	0.601(19)	0.592(18)	0.582(17)
	5	0.552(19)	0.5538(86)	0.5491(82)	0.514(17)	0.557(20)	0.549(21)	0.538(18)
	6	0.510(20)	0.514(10)	0.5084(86)	0.478(17)	0.516(25)	0.508(25)	0.499(20)
	8	0.445(27)	0.461(10)	0.4602(87)	0.428(22)	0.456(23)	0.453(22)	0.455(19)
	9	0.425(23)	0.431(12)	0.4322(92)	0.407(17)	0.429(26)	0.425(25)	0.433(19)
	10	0.409(28)	0.438(10)	0.4317(92)	0.393(25)	0.422(23)	0.419(22)	0.428(17)
$g_\perp$	1	0.801(23)	0.790(14)	0.785(14)	0.777(21)	0.824(23)	0.814(23)	0.789(21)
	2	0.714(24)	0.705(14)	0.699(17)	0.683(21)	0.733(24)	0.725(23)	0.705(21)
	3	0.652(24)	0.640(16)	0.635(18)	0.614(22)	0.663(24)	0.654(23)	0.641(22)
	4	0.594(23)	0.597(13)	0.587(12)	0.556(21)	0.594(24)	0.586(23)	0.578(21)
	5	0.548(23)	0.552(12)	0.546(11)	0.509(21)	0.550(25)	0.542(25)	0.535(23)
	6	0.506(23)	0.513(14)	0.507(12)	0.476(21)	0.507(31)	0.499(30)	0.496(26)
	8	0.443(35)	0.462(15)	0.461(13)	0.427(28)	0.448(32)	0.444(30)	0.453(26)
	9	0.423(32)	0.433(19)	0.434(14)	0.412(24)	0.415(39)	0.412(37)	0.429(29)
	10	0.405(40)	0.440(15)	0.433(13)	0.393(34)	0.417(34)	0.414(32)	0.429(25)
g_0	1	1.200(25)	1.184(24)	1.172(19)	1.178(24)	1.208(32)	1.184(32)	1.146(24)
	2	1.022(34)	1.009(26)	1.014(22)	1.020(20)	1.050(29)	1.038(30)	1.008(22)
	3	0.897(17)	0.885(13)	0.892(13)	0.880(14)	0.941(17)	0.931(14)	0.900(11)
	4	0.808(14)	0.802(12)	0.801(11)	0.795(19)	0.843(17)	0.834(12)	0.8090(91)
	5	0.725(13)	0.722(11)	0.726(10)	0.710(12)	0.768(12)	0.760(11)	0.7370(82)
	6	0.656(13)	0.652(11)	0.655(10)	0.634(11)	0.694(12)	0.690(11)	0.6705(88)
	8	0.553(13)	0.563(11)	0.567(10)	0.526(12)	0.597(12)	0.594(11)	0.5800(92)
	9	0.520(13)	0.517(11)	0.523(12)	0.479(11)	0.556(12)	0.554(12)	0.5451(95)
	10	0.492(14)	0.510(14)	0.506(16)	0.465(15)	0.527(14)	0.523(13)	0.518(10)

TABLE XIII. Lattice results for the vector and axial vector current helicity form factors.

	$\|\mathbf{p}'\|^2/(2\pi/L)^2$	C14	C24	C54	C53	F23	F43	F63
h_+	1	1.402(37)	1.391(31)	1.393(34)	1.358(32)	1.437(42)	1.403(46)	1.378(35)
	2	1.247(36)	1.230(28)	1.242(26)	1.210(28)	1.270(36)	1.268(31)	1.252(23)
	3	1.106(65)	1.096(50)	1.106(45)	1.076(49)	1.134(59)	1.137(51)	1.125(33)
	4	0.999(46)	0.992(33)	0.995(30)	0.980(28)	1.055(40)	1.037(35)	1.014(25)
	5	0.905(46)	0.901(31)	0.909(29)	0.884(30)	0.953(42)	0.947(36)	0.935(26)
	6	0.821(42)	0.821(32)	0.826(30)	0.795(39)	0.866(42)	0.865(35)	0.854(25)
	8	0.678(32)	0.685(23)	0.695(24)	0.668(28)	0.733(28)	0.731(27)	0.728(20)
	9	0.628(32)	0.631(23)	0.640(23)	0.604(25)	0.687(27)	0.686(27)	0.678(20)
	10	0.608(33)	0.618(25)	0.616(25)	0.601(31)	0.669(30)	0.663(29)	0.659(21)
$h_\perp$	1	1.074(23)	1.054(22)	1.052(22)	1.043(21)	1.101(27)	1.076(24)	1.055(18)
	2	0.938(21)	0.919(16)	0.922(17)	0.913(17)	0.960(21)	0.952(17)	0.939(13)
	3	0.829(40)	0.817(28)	0.819(27)	0.808(32)	0.850(36)	0.847(27)	0.837(19)
	4	0.750(21)	0.740(14)	0.739(12)	0.729(14)	0.786(17)	0.772(13)	0.757(10)
	5	0.678(19)	0.674(12)	0.676(11)	0.662(14)	0.712(16)	0.706(13)	0.693(11)
	6	0.618(18)	0.616(11)	0.616(11)	0.600(15)	0.651(14)	0.647(12)	0.638(10)
	8	0.522(18)	0.528(12)	0.531(11)	0.517(14)	0.559(14)	0.555(12)	0.5514(91)
	9	0.489(18)	0.487(12)	0.490(11)	0.474(14)	0.524(14)	0.520(12)	0.5170(91)
	10	0.464(19)	0.476(14)	0.471(12)	0.462(17)	0.502(19)	0.497(13)	0.496(10)
$\widetilde{h}_+$	1	0.772(16)	0.759(13)	0.756(15)	0.749(17)	0.795(14)	0.785(12)	0.762(14)
	2	0.685(20)	0.675(13)	0.672(16)	0.661(19)	0.702(15)	0.694(13)	0.680(18)
	3	0.634(15)	0.620(14)	0.617(15)	0.602(17)	0.644(15)	0.637(14)	0.623(15)
	4	0.583(17)	0.575(14)	0.567(15)	0.540(20)	0.604(15)	0.588(14)	0.573(16)
	5	0.540(16)	0.529(14)	0.525(15)	0.503(19)	0.553(16)	0.542(15)	0.533(16)
	6	0.495(18)	0.500(17)	0.494(18)	0.477(20)	0.509(19)	0.497(17)	0.493(17)
	8	0.451(18)	0.467(20)	0.464(20)	0.451(17)	0.462(21)	0.458(20)	0.466(17)
	9	0.436(26)	0.443(14)	0.442(14)	0.437(16)	0.441(28)	0.434(28)	0.449(19)
	10	0.421(21)	0.446(11)	0.440(12)	0.418(21)	0.453(19)	0.439(17)	0.446(15)
$\widetilde{h}_\perp$	1	0.772(16)	0.758(12)	0.755(14)	0.748(17)	0.794(13)	0.784(12)	0.762(14)
	2	0.685(20)	0.675(12)	0.672(15)	0.660(18)	0.701(14)	0.694(13)	0.680(17)
	3	0.633(15)	0.619(11)	0.616(12)	0.602(15)	0.643(14)	0.635(13)	0.622(13)
	4	0.585(16)	0.575(12)	0.567(13)	0.543(17)	0.601(17)	0.587(13)	0.575(14)
	5	0.539(15)	0.527(13)	0.524(13)	0.503(16)	0.551(14)	0.541(14)	0.531(15)
	6	0.490(17)	0.494(16)	0.489(17)	0.474(17)	0.504(17)	0.493(16)	0.490(16)
	8	0.442(17)	0.457(17)	0.455(17)	0.442(14)	0.454(17)	0.450(16)	0.459(14)
	9	0.422(24)	0.428(13)	0.428(13)	0.423(15)	0.428(28)	0.423(28)	0.438(18)
	10	0.410(21)	0.4320(89)	0.4271(99)	0.406(19)	0.439(16)	0.428(15)	0.436(13)

TABLE XIV. Lattice results for the tensor current helicity form factors.

	$\|\mathbf{p}'\|^2/(2\pi/L)^2$	C14	C24	C54	C53	F23	F43	F63
f_1^V	1	0.995(24)	0.983(20)	0.976(19)	0.958(21)	1.017(26)	1.005(21)	0.987(17)
	2	0.855(32)	0.850(22)	0.847(22)	0.839(17)	0.879(23)	0.874(20)	0.865(22)
	3	0.769(32)	0.762(21)	0.761(23)	0.740(24)	0.787(33)	0.785(26)	0.778(24)
	4	0.707(31)	0.707(16)	0.701(14)	0.668(18)	0.746(25)	0.732(16)	0.7157(99)
	5	0.646(17)	0.645(11)	0.643(11)	0.6073(99)	0.676(15)	0.668(12)	0.6555(84)
	6	0.594(16)	0.596(10)	0.594(11)	0.5634(88)	0.620(13)	0.615(10)	0.6129(78)
	8	0.515(17)	0.530(11)	0.529(11)	0.490(10)	0.544(14)	0.540(11)	0.5427(84)
	9	0.488(17)	0.492(11)	0.492(12)	0.456(11)	0.512(14)	0.507(11)	0.5118(87)
	10	0.458(18)	0.483(13)	0.477(13)	0.429(17)	0.487(14)	0.485(12)	0.4949(87)
f_2^V	1	0.399(19)	0.397(17)	0.404(17)	0.384(24)	0.410(28)	0.398(30)	0.388(22)
	2	0.365(18)	0.354(16)	0.369(14)	0.359(19)	0.369(24)	0.368(20)	0.366(14)
	3	0.319(31)	0.317(21)	0.326(17)	0.324(31)	0.330(30)	0.328(25)	0.326(15)
	4	0.266(24)	0.261(20)	0.272(16)	0.269(17)	0.287(26)	0.286(21)	0.282(16)
	5	0.223(12)	0.222(10)	0.2328(93)	0.231(14)	0.237(15)	0.242(15)	0.244(10)
	6	0.202(12)	0.199(10)	0.2081(91)	0.209(14)	0.217(15)	0.223(15)	0.218(10)
	8	0.163(12)	0.162(10)	0.1714(94)	0.158(16)	0.179(16)	0.183(16)	0.183(11)
	9	0.147(13)	0.147(10)	0.1547(93)	0.135(15)	0.164(16)	0.169(16)	0.166(11)
	10	0.142(14)	0.140(12)	0.145(11)	0.132(21)	0.161(21)	0.160(18)	0.155(13)
f_3^V	1	−0.176(40)	−0.185(39)	−0.187(43)	−0.170(65)	−0.162(37)	−0.165(38)	−0.174(43)
	2	−0.120(25)	−0.119(23)	−0.128(22)	−0.137(44)	−0.118(28)	−0.124(24)	−0.133(22)
	3	−0.089(24)	−0.092(23)	−0.100(22)	−0.100(30)	−0.093(27)	−0.101(24)	−0.108(20)
	4	−0.078(34)	−0.087(37)	−0.094(33)	−0.098(36)	−0.107(52)	−0.105(36)	−0.095(21)
	5	−0.067(21)	−0.065(20)	−0.070(18)	−0.070(29)	−0.108(27)	−0.105(22)	−0.091(18)
	6	−0.057(22)	−0.053(21)	−0.061(19)	−0.059(30)	−0.093(27)	−0.096(23)	−0.087(20)
	8	−0.050(29)	−0.046(25)	−0.048(20)	−0.036(32)	−0.084(30)	−0.081(26)	−0.063(22)
	9	−0.037(34)	−0.032(26)	−0.035(21)	−0.011(31)	−0.082(33)	−0.080(29)	−0.051(23)
	10	−0.028(26)	−0.020(25)	−0.021(21)	−0.013(34)	−0.065(34)	−0.062(30)	−0.044(25)
f_1^A	1	0.817(13)	0.803(13)	0.804(12)	0.781(16)	0.837(17)	0.832(14)	0.777(12)
	2	0.726(11)	0.717(12)	0.716(10)	0.709(15)	0.757(18)	0.750(17)	0.707(12)
	3	0.664(11)	0.648(10)	0.6497(96)	0.631(12)	0.692(15)	0.686(13)	0.650(13)
	4	0.6139(89)	0.6119(85)	0.6106(84)	0.5823(92)	0.630(18)	0.626(13)	0.5981(61)
	5	0.5660(80)	0.5609(96)	0.5600(80)	0.5349(87)	0.5846(87)	0.5789(72)	0.5521(49)
	6	0.520(11)	0.5160(77)	0.5140(77)	0.4858(85)	0.541(10)	0.5355(98)	0.5111(73)
	8	0.450(12)	0.4589(78)	0.4583(76)	0.430(11)	0.475(11)	0.4710(99)	0.4588(72)
	9	0.4298(97)	0.4279(77)	0.4290(87)	0.3976(83)	0.455(10)	0.4515(96)	0.4404(67)
	10	0.416(12)	0.435(10)	0.429(13)	0.392(14)	0.431(12)	0.428(11)	0.4256(72)
f_2^A	1	0.021(25)	0.017(23)	0.024(22)	0.005(27)	0.017(31)	0.023(30)	−0.015(29)
	2	0.015(24)	0.015(24)	0.022(27)	0.034(36)	0.030(31)	0.032(32)	0.002(33)
	3	0.015(24)	0.011(27)	0.019(29)	0.022(32)	0.038(35)	0.041(36)	0.013(38)
	4	0.026(24)	0.020(22)	0.031(21)	0.034(26)	0.045(30)	0.051(29)	0.025(29)
	5	0.023(23)	0.011(21)	0.018(20)	0.033(25)	0.044(28)	0.048(29)	0.022(30)
	6	0.017(24)	0.004(23)	0.009(22)	0.013(26)	0.043(32)	0.046(32)	0.020(31)
	8	0.009(32)	−0.005(25)	−0.003(22)	0.004(28)	0.034(39)	0.034(38)	0.007(32)
	9	0.009(32)	−0.007(29)	−0.006(25)	−0.018(29)	0.050(47)	0.050(45)	0.015(39)
	10	0.015(40)	−0.007(26)	−0.005(24)	−0.002(35)	0.018(39)	0.017(38)	−0.004(32)
f_3^A	1	−0.787(44)	−0.793(46)	−0.778(32)	−0.816(48)	−0.753(61)	−0.727(61)	−0.774(38)
	2	−0.639(71)	−0.637(69)	−0.657(57)	−0.669(53)	−0.624(81)	−0.623(87)	−0.662(61)
	3	−0.527(33)	−0.541(27)	−0.560(19)	−0.560(28)	−0.554(33)	−0.554(30)	−0.572(20)
	4	−0.458(27)	−0.454(25)	−0.461(19)	−0.501(45)	−0.497(32)	−0.491(30)	−0.506(21)
	5	−0.394(23)	−0.403(22)	−0.420(17)	−0.431(28)	−0.448(30)	−0.447(29)	−0.464(20)
	6	−0.351(23)	−0.357(22)	−0.374(16)	−0.384(26)	−0.391(28)	−0.400(28)	−0.418(20)
	8	−0.295(24)	−0.299(23)	−0.317(18)	−0.271(27)	−0.344(32)	−0.349(31)	−0.348(21)
	9	−0.271(25)	−0.270(23)	−0.288(18)	−0.240(27)	−0.301(31)	−0.306(31)	−0.315(22)
	10	−0.237(27)	−0.238(26)	−0.245(21)	−0.229(40)	−0.298(38)	−0.298(36)	−0.293(27)

TABLE XV. Lattice results for the vector and axial vector current Weinberg form factors.

	$\|\mathbf{p}'\|^2/(2\pi/L)^2$	C14	C24	C54	C53	F23	F43	F63
f_1^{TV}	1	0.451(24)	0.458(22)	0.456(21)	0.432(23)	0.468(33)	0.447(36)	0.434(29)
	2	0.412(23)	0.411(21)	0.415(19)	0.398(20)	0.419(29)	0.420(26)	0.410(17)
	3	0.360(34)	0.359(29)	0.365(23)	0.348(24)	0.372(34)	0.375(33)	0.367(20)
	4	0.316(33)	0.315(26)	0.316(23)	0.318(22)	0.344(35)	0.334(31)	0.320(20)
	5	0.280(34)	0.278(26)	0.282(24)	0.274(24)	0.301(36)	0.298(30)	0.294(19)
	6	0.245(30)	0.245(25)	0.248(23)	0.236(29)	0.262(35)	0.263(29)	0.258(18)
	8	0.180(20)	0.181(17)	0.188(16)	0.176(20)	0.203(22)	0.204(23)	0.202(16)
	9	0.158(20)	0.163(17)	0.167(16)	0.148(17)	0.187(22)	0.189(22)	0.182(15)
	10	0.161(21)	0.158(18)	0.159(17)	0.155(22)	0.187(24)	0.186(24)	0.181(17)
f_2^{TV}	1	0.855(20)	0.833(19)	0.836(17)	0.833(20)	0.871(26)	0.860(19)	0.849(15)
	2	0.747(16)	0.731(14)	0.734(14)	0.728(16)	0.763(19)	0.758(14)	0.752(12)
	3	0.669(26)	0.659(17)	0.661(19)	0.653(24)	0.684(25)	0.681(16)	0.677(13)
	4	0.616(11)	0.6083(80)	0.6088(71)	0.5942(94)	0.638(13)	0.6312(94)	0.6233(73)
	5	0.565(11)	0.5634(74)	0.5641(68)	0.5508(93)	0.589(11)	0.5854(86)	0.5759(52)
	6	0.523(10)	0.5221(67)	0.5227(60)	0.5090(77)	0.5493(82)	0.5460(55)	0.5391(44)
	8	0.459(11)	0.4647(77)	0.4662(67)	0.454(10)	0.4870(92)	0.4834(66)	0.4811(57)
	9	0.437(11)	0.4327(78)	0.4350(68)	0.424(10)	0.4608(93)	0.4563(67)	0.4566(57)
	10	0.413(18)	0.426(12)	0.4219(89)	0.413(15)	0.442(22)	0.437(14)	0.4387(89)
f_1^{TA}	1	0.010(20)	0.018(19)	0.021(17)	0.011(25)	0.043(33)	0.027(33)	0.009(19)
	2	0.000(17)	0.005(18)	0.005(18)	0.003(21)	0.014(22)	0.012(20)	0.008(17)
	3	0.004(24)	0.010(30)	0.008(29)	0.003(28)	0.013(25)	0.014(21)	0.006(30)
	4	−0.017(27)	−0.002(24)	−0.003(21)	−0.020(26)	0.021(37)	0.006(37)	−0.011(22)
	5	0.008(17)	0.016(17)	0.012(16)	0.000(23)	0.012(22)	0.011(20)	0.011(17)
	6	0.024(18)	0.031(17)	0.024(16)	0.015(23)	0.027(26)	0.022(21)	0.017(17)
	8	0.037(17)	0.044(15)	0.037(16)	0.038(19)	0.033(26)	0.030(24)	0.031(21)
	9	0.053(13)	0.057(13)	0.051(13)	0.054(15)	0.047(20)	0.042(18)	0.043(14)
	10	0.040(15)	0.049(14)	0.046(14)	0.039(20)	0.047(23)	0.036(20)	0.035(16)
f_2^{TA}	1	0.764(22)	0.745(15)	0.739(16)	0.740(22)	0.761(28)	0.763(26)	0.755(23)
	2	0.685(22)	0.672(10)	0.6681(94)	0.658(13)	0.691(17)	0.685(15)	0.674(10)
	3	0.631(17)	0.612(15)	0.611(11)	0.600(12)	0.634(20)	0.626(16)	0.618(12)
	4	0.596(17)	0.577(14)	0.5695(97)	0.556(12)	0.588(34)	0.583(28)	0.582(11)
	5	0.534(15)	0.517(11)	0.516(11)	0.503(14)	0.543(16)	0.534(15)	0.524(13)
	6	0.476(18)	0.476(13)	0.475(14)	0.465(15)	0.487(19)	0.480(19)	0.479(15)
	8	0.422(18)	0.433(13)	0.435(11)	0.421(13)	0.437(19)	0.434(18)	0.442(12)
	9	0.394(22)	0.398(13)	0.402(12)	0.395(14)	0.404(29)	0.401(29)	0.416(17)
	10	0.390(21)	0.4081(95)	0.4045(88)	0.387(18)	0.416(18)	0.410(17)	0.418(11)

TABLE XVI. Lattice results for the tensor current Weinberg form factors.

[1] T. Blake, T. Gershon, and G. Hiller, "Rare b hadron decays at the LHC," Ann. Rev. Nucl. Part. Sci. **65**, 113–143 (2015), arXiv:1501.03309 [hep-ex].

[2] S. Descotes-Genon, J. Matias, and J. Virto, "Understanding the $B \to K^* \mu^+ \mu^-$ Anomaly," Phys. Rev. **D88**, 074002 (2013), arXiv:1307.5683 [hep-ph].

[3] **LHCb** Collaboration, R. Aaij *et al.*, "Measurement of Form-Factor-Independent Observables in the Decay $B^0 \to K^{*0} \mu^+ \mu^-$," Phys. Rev. Lett. **111**, 191801 (2013), arXiv:1308.1707 [hep-ex].

[4] **LHCb** Collaboration, R. Aaij *et al.*, "Angular analysis of the $B^0 \to K^{*0} \mu^+ \mu^-$ decay," arXiv:1512.04442 [hep-ex].

[5] **HPQCD** Collaboration, C. Bouchard, G. P. Lepage, C. Monahan, H. Na, and J. Shigemitsu, "Standard Model Predictions for $B \to K \ell^+ \ell^-$ with Form Factors from Lattice QCD," Phys. Rev. Lett. **111**, 162002 (2013), arXiv:1306.0434 [hep-ph]. [Erratum: Phys. Rev. Lett. **112**, 149902 (2014)].

[6] R. R. Horgan, Z. Liu, S. Meinel, and M. Wingate, "Calculation of $B^0 \to K^{*0} \mu^+ \mu^-$ and $B_s^0 \to \phi \mu^+ \mu^-$ observables using form factors from lattice QCD," Phys. Rev. Lett. **112**, 212003 (2014), arXiv:1310.3887 [hep-ph].

[7] A. Bharucha, D. M. Straub, and R. Zwicky, "$B \to V \ell^+ \ell^-$ in the Standard Model from Light-Cone Sum Rules," arXiv:1503.05534 [hep-ph].

[8] D. Du, A. X. El-Khadra, S. Gottlieb, A. S. Kronfeld, J. Laiho, E. Lunghi, R. S. Van de Water, and R. Zhou, "Phenomenology of Semileptonic B-Meson Decays with Form Factors from Lattice QCD," arXiv:1510.02349 [hep-ph].

[9] **LHCb** Collaboration, R. Aaij *et al.*, "Differential branching fraction and angular analysis of the decay $B^0 \to K^{*0} \mu^+ \mu^-$," JHEP **08**, 131 (2013), arXiv:1304.6325.

[10] **LHCb** Collaboration, R. Aaij *et al.*, "Differential branching fraction and angular analysis of the decay $B_s^0 \to \phi \mu^+ \mu^-$," JHEP **07**, 084 (2013), arXiv:1305.2168 [hep-ex].

[11] **LHCb** Collaboration, R. Aaij *et al.*, "Angular analysis and differential branching fraction of the decay $B_s^0 \to \phi \mu^+ \mu^-$," JHEP **09**, 179 (2015), arXiv:1506.08777 [hep-ex].

[12] **LHCb** Collaboration, R. Aaij *et al.*, "Test of lepton universality using $B^+ \to K^+ \ell^+ \ell^-$ decays," Phys. Rev. Lett. **113**, 151601 (2014), arXiv:1406.6482 [hep-ex].

[13] W. Altmannshofer and D. M. Straub, "New physics in $b \to s$ transitions after LHC run 1," Eur. Phys. J. **C75** no. 8, 382 (2015), arXiv:1411.3161 [hep-ph].

[14] S. Descotes-Genon, L. Hofer, J. Matias, and J. Virto, "Global analysis of $b \to s \ell\ell$ anomalies," arXiv:1510.04239 [hep-ph].

[15] W. Detmold, C.-J. D. Lin, S. Meinel, and M. Wingate, "$\Lambda_b \to \Lambda \ell^+ \ell^-$ form factors and differential branching fraction from lattice QCD," Phys. Rev. **D87**, 074502 (2013), arXiv:1212.4827 [hep-lat].

[16] **HPQCD** Collaboration, C. Bouchard, G. P. Lepage, C. Monahan, H. Na, and J. Shigemitsu, "Rare decay $B \to K \ell^+ \ell^-$ form factors from lattice QCD," Phys. Rev. **D88**, 054509 (2013), arXiv:1306.2384 [hep-lat]. [Erratum: Phys. Rev. **D88**, 079901 (2013)].

[17] R. R. Horgan, Z. Liu, S. Meinel, and M. Wingate, "Lattice QCD calculation of form factors describing the rare decays $B \to K^* \ell^+ \ell^-$ and $B_s \to \phi \ell^+ \ell^-$," Phys. Rev. **D89**, 094501 (2014), arXiv:1310.3722 [hep-lat].

[18] J. A. Bailey *et al.*, "$B \to K l^+ l^-$ decay form factors from three-flavor lattice QCD," arXiv:1509.06235 [hep-lat].

[19] B. Grinstein and D. Pirjol, "Exclusive rare $B \to K^* \ell^+ \ell^-$ decays at low recoil: Controlling the long-distance effects," Phys. Rev. **D70** 114005, (2004), arXiv:hep-ph/0404250.

[20] M. Beylich, G. Buchalla, and T. Feldmann, "Theory of $B \to K^{(*)} \ell^+ \ell^-$ decays at high q^2: OPE and quark-hadron duality," Eur. Phys. J. **C71**, 1635 (2011), arXiv:1101.5118 [hep-ph].

[21] M. Beneke, T. Feldmann, and D. Seidel, "Systematic approach to exclusive $B \to V \ell^+ \ell^-, V \gamma$ decays," Nucl. Phys. **B612**, 25–58 (2001), arXiv:hep-ph/0106067.

[22] A. Khodjamirian, T. Mannel, A. A. Pivovarov, and Y. M. Wang, "Charm-loop effect in $B \to K^{(*)} \ell^+ \ell^-$ and $B \to K^* \gamma$," JHEP **09**, 089 (2010), arXiv:1006.4945 [hep-ph].

[23] A. Khodjamirian, T. Mannel, and Y. M. Wang, "$B \to K \ell^+ \ell^-$ decay at large hadronic recoil," JHEP **02**, 010 (2013), arXiv:1211.0234 [hep-ph].

[24] J. Lyon and R. Zwicky, "Resonances gone topsy turvy - the charm of QCD or new physics in $b \to s \ell^+ \ell^-$?," arXiv:1406.0566 [hep-ph].

[25] W. Altmannshofer and D. M. Straub, "Implications of $b \to s$ measurements," in *Proceedings, 50th Recontres de Moriond Electroweak interactions and unified theories*, pp. 333–338. 2015. arXiv:1503.06199 [hep-ph]. http://inspirehep.net/record/1353682/files/arXiv:1503.06199.pdf.

[26] **CDF** Collaboration, T. Aaltonen *et al.*, "Observation of the Baryonic Flavor-Changing Neutral Current Decay $\Lambda_b \to \Lambda \mu^+ \mu^-$," Phys. Rev. Lett. **107**, 201802 (2011), arXiv:1107.3753 [hep-ex].

[27] **LHCb** Collaboration, R. Aaij *et al.*, "Measurement of the differential branching fraction of the decay $\Lambda_b^0 \to \Lambda \mu^+ \mu^-$," Phys. Lett. **B725**, 25–35 (2013), arXiv:1306.2577 [hep-ex].

[28] **LHCb** Collaboration, R. Aaij *et al.*, "Differential branching fraction and angular analysis of $\Lambda_b^0 \to \Lambda \mu^+ \mu^-$ decays," JHEP **06**, 115 (2015), arXiv:1503.07138 [hep-ex].

[29] T. Gutsche, M. A. Ivanov, J. G. Körner, V. E. Lyubovitskij, and P. Santorelli, "Rare baryon decays $\Lambda_b \to \Lambda l^+ l^- (l = e, \mu, \tau)$ and $\Lambda_b \to \Lambda \gamma$: differential and total rates, lepton- and hadron-side forward-backward asymmetries," Phys. Rev. **D87**, 074031 (2013), arXiv:1301.3737 [hep-ph].

[30] P. Böer, T. Feldmann, and D. van Dyk, "Angular Analysis of the Decay $\Lambda_b \to \Lambda(\to N\pi)\ell^+\ell^-$," JHEP **01**, 155 (2015), arXiv:1410.2115 [hep-ph].

[31] M. Gremm, F. Kruger, and L. M. Sehgal, "Angular distribution and polarization of photons in the inclusive decay $\Lambda_b \to X_s\gamma$," Phys. Lett. **B355**, 579–583 (1995), arXiv:hep-ph/9505354.

[32] T. Mannel and S. Recksiegel, "Flavor changing neutral current decays of heavy baryons: The Case $\Lambda_b \to \Lambda\gamma$," J. Phys. **G24**, 979–990 (1998) , arXiv:hep-ph/9701399.

[33] C.-K. Chua, X.-G. He, and W.-S. Hou, "CP violating $b \to s\gamma$ decay in supersymmetric models," Phys. Rev. **D60**, 014003 (1999), arXiv:hep-ph/9808431.

[34] C.-S. Huang and H.-G. Yan, "Exclusive rare decays of heavy baryons to light baryons: $\Lambda_b \to \Lambda\gamma$ and $\Lambda_b \to \Lambda\ell^+\ell^-$," Phys. Rev. **D59**, 114022 (1999), arXiv:hep-ph/9811303. [Erratum: Phys. Rev. **D61**, 039901 (2000)].

[35] G. Hiller and A. Kagan, "Probing for new physics in polarized Λ_b decays at the Z," Phys. Rev. **D65**, 074038 (2002), arXiv:hep-ph/0108074.

[36] C.-H. Chen and C. Q. Geng, "Rare $\Lambda_b \to \Lambda\ell^+\ell^-$ decays with polarized Λ," Phys. Rev. **D63**, 114024 (2001), arXiv:hep-ph/0101171.

[37] C.-H. Chen, C. Q. Geng, and J. N. Ng, "T violation in $\Lambda_b \to \Lambda\ell^+\ell^-$ decays with polarized Λ," Phys. Rev. **D65**, 091502 (2002), arXiv:hep-ph/0202103.

[38] T. M. Aliev and M. Savci, "Polarization effects in exclusive semileptonic $\Lambda_b \to \Lambda\ell^+\ell^-$," JHEP **05**, 001 (2006), arXiv:hep-ph/0507324.

[39] Y.-m. Wang, Y. Li, and C.-D. Lu, "Rare Decays of $\Lambda_b \to \Lambda\gamma$ and $\Lambda_b \to \Lambda\ell^+\ell^-$ in the Light-cone Sum Rules," Eur. Phys. J. **C59**, 861–882 (2009), arXiv:0804.0648 [hep-ph].

[40] M. J. Aslam, Y.-M. Wang, and C.-D. Lu, "Exclusive semileptonic decays of $\Lambda_b \to \Lambda\ell^+\ell^-$ in supersymmetric theories," Phys. Rev. **D78**, 114032 (2008), arXiv:0808.2113 [hep-ph].

[41] T. Mannel and Y.-M. Wang, "Heavy-to-light baryonic form factors at large recoil," JHEP **12**, 067 (2011), arXiv:1111.1849 [hep-ph].

[42] K. Azizi, A. T. Olgun, and Z. Tavukoglu, "Comparative analysis of the $\Lambda_b \to \Lambda\ell^+\ell^-$ decay in the SM, SUSY and RS model with custodial protection," arXiv:1508.03980 [hep-ph].

[43] L. Mott and W. Roberts, "Lepton polarization asymmetries for FCNC decays of the Λ_b baryon," Int. J. Mod. Phys. **A30** no. 27, 1550172 (2015), arXiv:1506.04106 [nucl-th].

[44] G. Kumar and N. Mahajan, "Asymmetries and observables for $\Lambda_b \to \Lambda\ell^+\ell^-$," arXiv:1511.00935 [hep-ph].

[45] L. Lellouch and M. Luscher, "Weak transition matrix elements from finite volume correlation functions," Commun. Math. Phys. **219**, 31–44 (2001), arXiv:hep-lat/0003023.

[46] R. A. Briceno, M. T. Hansen, and A. Walker-Loud, "Multichannel $1 \to 2$ transition amplitudes in a finite volume," Phys. Rev. **D91**, 034501 (2015), arXiv:1406.5965 [hep-lat].

[47] R. A. Briceno and M. T. Hansen, "Multichannel $0 \to 2$ and $1 \to 2$ transition amplitudes for arbitrary spin particles in a finite volume," Phys. Rev. **D92**, 074509 (2015), arXiv:1502.04314 [hep-lat].

[48] **LHCb** Collaboration, R. Aaij *et al.*, "Measurements of the $\Lambda_b^0 \to J/\psi\Lambda$ decay amplitudes and the Λ_b^0 polarisation in pp collisions at $\sqrt{s} = 7$ TeV," Phys. Lett. **B724**, 27–35 (2013), arXiv:1302.5578 [hep-ex].

[49] J. G. Körner, "Helicity Amplitudes and Angular Decay Distributions," in *Proceedings, Helmholtz International Summer School on Physics of Heavy Quarks and Hadrons (HQ 2013)*, pp. 169–184. 2014. arXiv:1402.2787 [hep-ph]. http://inspirehep.net/record/1281073/files/arXiv:1402.2787.pdf.

[50] T. Mannel, W. Roberts, and Z. Ryzak, "Baryons in the heavy quark effective theory," Nucl. Phys. **B355**, 38–53 (1991).

[51] F. Hussain, J. Körner, M. Kramer, and G. Thompson, "On heavy baryon decay form-factors," Z. Phys. **C51**, 321–328 (1991).

[52] F. Hussain, D.-S. Liu, M. Kramer, J. Körner, and S. Tawfiq, "General analysis of weak decay form-factors in heavy to heavy and heavy to light baryon transitions," Nucl. Phys. **B370**, 259–277 (1992).

[53] H.-Y. Cheng, C.-Y. Cheung, G.-L. Lin, Y. C. Lin, T.-M. Yan, and H.-L. Yu, "Effective Lagrangian approach to weak radiative decays of heavy hadrons," Phys. Rev. **D51**, 1199–1214 (1995), arXiv:hep-ph/9407303.

[54] H.-Y. Cheng and B. Tseng, "$1/M$ corrections to baryonic form-factors in the quark model," Phys. Rev. **D53**, 1457 (1996), arXiv:hep-ph/9502391. [Erratum: Phys. Rev. **D55**, 1697 (1997)].

[55] R. Mohanta, A. K. Giri, M. P. Khanna, M. Ishida, and S. Ishida, "Weak radiative decay $\Lambda_b \to \Lambda\gamma$ and quark confined effects in the covariant oscillator quark model," Prog. Theor. Phys. **102**, 645–652 (1999), arXiv:hep-ph/9908291.

[56] X.-G. He, T. Li, X.-Q. Li, and Y.-M. Wang, "PQCD calculation for $\Lambda_b \to \Lambda\gamma$ in the standard model," Phys. Rev. **D74**, 034026 (2006), arXiv:hep-ph/0606025.

[57] Y.-M. Wang, Y.-L. Shen, and C.-D. Lu, "$\Lambda_b \to p, \Lambda$ transition form factors from QCD light-cone sum rules," Phys. Rev. **D80**, 074012 (2009), arXiv:0907.4008 [hep-ph].

[58] L. Mott and W. Roberts, "Rare dileptonic decays of Λ_b in a quark model," Int. J. Mod. Phys. **A27**, 1250016 (2012), arXiv:1108.6129 [nucl-th].

[59] T. Feldmann and M. W. Yip, "Form Factors for $\Lambda_b \to \Lambda$ Transitions in SCET," Phys. Rev. **D85**, 014035 (2012), arXiv:1111.1844 [hep-ph].

[60] W. Wang, "Factorization of Heavy-to-Light Baryonic Transitions in SCET," Phys. Lett. **B708**, 119–126 (2012), arXiv:1112.0237 [hep-ph].

[61] Y. Liu, X. H. Guo, and C. Wang, "Study of two body hadronic decays $\Lambda_b \to \Lambda(p)P(V)$ in the instantaneous approximation of the Bethe-Salpeter equation approach," Phys. Rev. **D91**, 016006 (2015).

[62] Y.-M. Wang and Y.-L. Shen, "Perturbative Corrections to $\Lambda_b \to \Lambda$ Form Factors from QCD Light-Cone Sum Rules," arXiv:1511.09036 [hep-ph].

[63] S. Meinel, "Flavor physics with Λ_b baryons," PoS **LATTICE2013** (2014) 024, arXiv:1401.2685 [hep-lat].

[64] A. X. El-Khadra, A. S. Kronfeld, and P. B. Mackenzie, "Massive fermions in lattice gauge theory," Phys. Rev. **D55**, 3933–3957 (1997), arXiv:hep-lat/9604004.

[65] S. Aoki, Y. Kuramashi, and S.-i. Tominaga, "Relativistic heavy quarks on the lattice," Prog. Theor. Phys. **109**, 383–413 (2003), arXiv:hep-lat/0107009.

[66] S. Aoki, Y. Kayaba, and Y. Kuramashi, "A Perturbative determination of mass dependent $O(a)$ improvement coefficients in a relativistic heavy quark action," Nucl. Phys. **B697**, 271–301 (2004), arXiv:hep-lat/0309161.

[67] H.-W. Lin and N. Christ, "Non-perturbatively Determined Relativistic Heavy Quark Action," Phys. Rev. **D76**, 074506 (2007), arXiv:hep-lat/0608005.

[68] **RBC, UKQCD** Collaboration, Y. Aoki *et al.*, "Nonperturbative tuning of an improved relativistic heavy-quark action with application to bottom spectroscopy," Phys. Rev. **D86**, 116003 (2012), arXiv:1206.2554 [hep-lat].

[69] W. Detmold, C. Lehner, and S. Meinel, "$\Lambda_b \to p\ell^-\bar{\nu}_\ell$ and $\Lambda_b \to \Lambda_c\ell^-\bar{\nu}_\ell$ form factors from lattice QCD with relativistic heavy quarks," Phys. Rev. **D92**, 034503 (2015), arXiv:1503.01421 [hep-lat].

[70] **LHCb** Collaboration, R. Aaij *et al.*, "Determination of the quark coupling strength $|V_{ub}|$ using baryonic decays," Nature Phys. **11**, 743–747 (2015), arXiv:1504.01568 [hep-ex].

[71] D. B. Kaplan, "A Method for simulating chiral fermions on the lattice," Phys. Lett. **B288**, 342–347 (1992), arXiv:hep-lat/9206013.

[72] V. Furman and Y. Shamir, "Axial symmetries in lattice QCD with Kaplan fermions," Nucl. Phys. **B439**, 54–78 (1995), arXiv:hep-lat/9405004.

[73] Y. Shamir, "Chiral fermions from lattice boundaries," Nucl. Phys. **B406**, 90–106 (1993), arXiv:hep-lat/9303005.

[74] **RBC, UKQCD** Collaboration, Y. Aoki *et al.*, "Continuum Limit Physics from 2+1 Flavor Domain Wall QCD," Phys. Rev. **D83**, 074508 (2011), arXiv:1011.0892 [hep-lat].

[75] S. Weinberg, "Charge symmetry of weak interactions," Phys. Rev. **112**, 1375–1379 (1958).

[76] W. Detmold, C. D. Lin, and S. Meinel, "Calculation of the heavy-hadron axial couplings g_1, g_2, and g_3 using lattice QCD," Phys. Rev. **D85**, 114508 (2012), arXiv:1203.3378 [hep-lat].

[77] S. Hashimoto, A. X. El-Khadra, A. S. Kronfeld, P. B. Mackenzie, S. M. Ryan, *et al.*, "Lattice QCD calculation of $\bar{B} \to D\ell\bar{\nu}$ decay form-factors at zero recoil," Phys. Rev. **D61**, 014502 (1999), arXiv:hep-ph/9906376.

[78] A. X. El-Khadra, A. S. Kronfeld, P. B. Mackenzie, S. M. Ryan, and J. N. Simone, "The Semileptonic decays $B \to \pi\ell\nu$ and $D \to \pi\ell\nu$ from lattice QCD," Phys. Rev. **D64**, 014502 (2001), arXiv:hep-ph/0101023.

[79] **HPQCD** Collaboration, C. T. H. Davies, E. Follana, I. D. Kendall, G. P. Lepage, and C. McNeile, "Precise determination of the lattice spacing in full lattice QCD," Phys. Rev. **D81**, 034506 (2010), arXiv:0910.1229 [hep-lat].

[80] **HPQCD** Collaboration, R. J. Dowdall *et al.*, "The Upsilon spectrum and the determination of the lattice spacing from lattice QCD including charm quarks in the sea," Phys. Rev. **D85**, 054509 (2012), arXiv:1110.6887 [hep-lat].

[81] S. Meinel, "Bottomonium spectrum at order v^6 from domain-wall lattice QCD: Precise results for hyperfine splittings," Phys. Rev. **D82**, 114502 (2010), arXiv:1007.3966 [hep-lat].

[82] C. Bourrely, I. Caprini, and L. Lellouch, "Model-independent description of $B \to \pi\ell\nu$ decays and a determination of $|V_{ub}|$," Phys. Rev. **D79**, 013008 (2009), arXiv:0807.2722 [hep-ph].

[83] C. G. Boyd and R. F. Lebed, "Improved QCD form-factor constraints and $\Lambda_b \to \Lambda_c\ell\bar{\nu}$," Nucl. Phys. **B485**, 275–290 (1997), arXiv:hep-ph/9512363.

[84] **Particle Data Group** Collaboration, K. Olive *et al.*, "Review of Particle Physics," Chin.Phys. **C38**, 090001 (2014).

[85] C. B. Lang, D. Mohler, S. Prelovsek, and R. M. Woloshyn, "Predicting positive parity B_s mesons from lattice QCD," Phys. Lett. **B750**, 17–21 (2015), arXiv:1501.01646 [hep-lat].

[86] C. Greub, V. Pilipp, and C. Schupbach, "Analytic calculation of two-loop QCD corrections to $b \to s\ell^+\ell^-$ in the high q^2 region," JHEP **12**, 040 (2008), arXiv:0810.4077 [hep-ph].

[87] H. H. Asatryan, H. M. Asatrian, C. Greub, and M. Walker, "Calculation of two loop virtual corrections to $b \to s\ell^+\ell^-$ in the standard model," Phys. Rev. **D65**, 074004 (2002), arXiv:hep-ph/0109140.

[88] C. Bobeth, M. Misiak, and J. Urban, "Photonic penguins at two loops and m_t-dependence of $BR[B \to X_s\ell^+\ell^-]$," Nucl. Phys. **B574**, 291–330 (2000), arXiv:hep-ph/9910220.

[89] P. Gambino, M. Gorbahn, and U. Haisch, "Anomalous dimension matrix for radiative and rare semileptonic B decays up to three loops," Nucl. Phys. **B673**, 238–262 (2003), arXiv:hep-ph/0306079.

[90] M. Gorbahn and U. Haisch, "Effective Hamiltonian for non-leptonic $|\Delta F| = 1$ decays at NNLO in QCD," Nucl. Phys. **B713**, 291–332 (2005), arXiv:hep-ph/0411071.

[91] M. Gorbahn, U. Haisch, and M. Misiak, "Three-loop mixing of dipole operators," Phys. Rev. Lett. **95**, 102004 (2005), arXiv:hep-ph/0504194.

[92] F. Beaujean, C. Bobeth, D. van Dyk, and C. Wacker, "Bayesian Fit of Exclusive $b \to s\bar{\ell}\ell$ Decays: The Standard Model Operator Basis," JHEP **08**, 030 (2012), arXiv:1205.1838 [hep-ph].

[93] **EOS Working Group** Collaboration. http://project.het.physik.tu-dortmund.de/eos/.

[94] **UTfit** Collaboration. http://www.utfit.org/UTfit/ResultsSummer2014PostMoriondSM.

[95] F. Jegerlehner, "Electroweak effective couplings for future precision experiments," Nuovo Cim. **C034S1**, 31–40 (2011), arXiv:1107.4683 [hep-ph].

[96] F. Jegerlehner. http://www-com.physik.hu-berlin.de/~fjeger/alphaQED.tar.gz.

[97] D. J. Broadhurst and A. G. Grozin, "Matching QCD and HQET heavy - light currents at two loops and beyond," Phys. Rev. **D52**, 4082–4098 (1995), arXiv:hep-ph/9410240.
[98] D. J. Gross and F. Wilczek, "Ultraviolet Behavior of Nonabelian Gauge Theories," Phys. Rev. Lett. **30**, 1343–1346 (1973).
[99] R. Lednicky, "On Evaluation of Polarization of the Charmed Baryon Λ_c (In Russian)," Sov. J. Nucl. Phys. **43**, 817 (1986). [Yad. Fiz. **43**, 1275 (1986)].
[100] **LHCb** Collaboration, A. A. Alves, Jr. *et al.*, "The LHCb Detector at the LHC," JINST **3**, S08005 (2008).
[101] **SciDAC, LHPC, UKQCD** Collaboration, R. G. Edwards and B. Joo, "The Chroma software system for lattice QCD," Nucl. Phys. Proc. Suppl. **140**, 832 (2005), arXiv:hep-lat/0409003.